



23 Correspondence: Yuming Jin (yumingjin@ucar.edu)



24 Abstract

25 Atmospheric Potential Oxygen (APO, defined as $O_2 + 1.1 \times CO_2$) is a tracer of air-sea O_2
26 exchange, exhibiting strong seasonal variability over mid-to-high latitudes. We present results
27 from the first version of Atmospheric Potential Oxygen forward Model Intercomparison Project
28 (APO-MIP1), which forward transports three air-sea APO flux products in eight atmospheric
29 transport models or model variants, aiming to evaluate atmospheric transport and flux
30 representations by comparing simulations against surface station, airborne, and shipboard
31 observations of APO. We find significant spread and bias in APO simulations at eastern Pacific
32 surface stations, indicating inconsistencies in representing vertical and coastal atmospheric
33 mixing. A framework using airborne APO observations demonstrates that most atmospheric
34 transport models (ATMs) participating in APO-MIP1 overestimate tracer diffusive mixing across
35 moist isentropes (i.e., diabatic mixing) in mid-latitudes. This framework also enables us to
36 isolate ATM-related biases in simulated APO distributions using independent mixing constraints
37 derived from moist static energy budgets from reanalysis, thereby allowing us to assess
38 large-scale features in air-sea APO flux products. Furthermore, shipboard observations show that
39 ATMs are unable to reproduce seasonal APO gradients over Drake Passage and near Palmer
40 Station, Antarctica, which could arise from uncertainties in APO fluxes or model transport. The
41 transport simulations and flux products from APO-MIP1 provide valuable resources for
42 developing new APO flux inversions and evaluating ocean biogeochemical processes.

43 Short Summary

44 We carry out a comprehensive atmospheric transport model (ATM) intercomparison project. This
45 project aims to evaluate errors in ATMs and three air-sea O_2 exchange products by comparing
46 model simulations with observations collected from surface stations, ships, and aircraft. We also
47 present a model evaluation framework to independently quantify transport-related and
48 flux-related biases that contribute to model-observation discrepancies in atmospheric tracer
49 distributions.



50 1. Introduction

51 Atmospheric potential oxygen (APO), defined as the weighted sum of O_2 and CO_2 concentration
52 ($APO = O_2 + 1.1 CO_2$), is an important tracer of fossil fuel burning and ocean biogeochemical
53 processes (Stephens et al., 1998). APO is intended to be unaffected by terrestrial photosynthesis
54 and respiration due to the cancellation of O_2 and CO_2 exchange at an approximate $O_2:C$ ratio of
55 -1.1 (Severinghaus, 1995). APO exhibits a large seasonal cycle driven mainly by air-sea O_2
56 exchange due to upper ocean biological activities, deep water ventilation, and thermally induced
57 O_2 solubility changes. Seasonal APO variability is also slightly affected by the air-sea exchange
58 of CO_2 and N_2 (Manning & Keeling, 2006). APO is decreasing in the atmosphere due to fossil
59 fuel combustion, which acts as an O_2 sink and CO_2 source with a more negative $O_2:CO_2$ ratio
60 (global mean ~ -1.4) compared to the assumed -1.1 ratio from terrestrial processes. Although
61 fossil fuel combustion contributes to an annual interhemispheric gradient that has lower APO in
62 the Northern Hemisphere, it has only a minor effect on the seasonal cycle globally (Keeling &
63 Manning, 2014).

64 APO measurements provide critical constraints on seasonal air-sea O_2 fluxes, which have been
65 used to estimate air-sea gas exchange rates and ocean net community production (NCP), and to
66 benchmark marine NCP in Earth system models (Keeling et al., 1998; Naegler et al., 2007;
67 Nevison et al., 2012, 2015, 2016, 2018). APO has been used for improved partitioning of ocean
68 and land carbon sinks (Friedlingstein et al., 2025; Manning & Keeling, 2006), to constrain ocean
69 heat uptake and meridional heat transport (Resplandy et al., 2016, 2019), and to quantify fossil
70 fuel emissions (Pickers et al., 2022; Rödenbeck et al., 2023). APO measurements are available at
71 surface stations (Adcock et al., 2023; Battle et al., 2006; Goto et al., 2017; Keeling & Manning,
72 2014; Manning & Keeling, 2006; Nguyen et al., 2022; Tohjima et al., 2019), on ship transects
73 (Ishidoya et al., 2016; Pickers et al., 2017; Stephens et al., 2003; Thompson et al., 2007; Tohjima
74 et al., 2012, 2015, 2024), and from aircraft (Bent, 2014; Ishidoya et al., 2012; Jin et al., 2023;
75 Langenfelds, 2002; Morgan et al., 2021; Stephens et al., 2018, 2021).

76 Global-scale air-sea APO fluxes have been estimated from APO measurements and an ATM
77 within a Bayesian inversion framework (Rödenbeck et al., 2008). ATMs are also used to forward
78 transport APO fluxes simulated from ocean biogeochemistry models (Carroll et al., 2020; Yeager
79 et al., 2022) and surface ocean dissolved oxygen (DO) measurements (Garcia & Keeling, 2001;



80 Najjar & Keeling, 2000) to compare with atmospheric observations, providing a basis for model
81 and flux product evaluation (Jin et al., 2023; Keeling et al., 1998; Stephens et al., 1998).
82 However, using atmospheric data to evaluate flux products and to derive fluxes through
83 inversion is fundamentally limited by biases in ATMs, particularly in their representation of
84 vertical transport and diabatic mixing (Jin et al., 2024; Naegler et al., 2007; Nevison et al., 2008;
85 Schuh et al., 2019; Schuh & Jacobson, 2023; Stephens et al., 2007). The systematic uncertainties
86 in transport modeling limit inversions of APO, CO₂, and other greenhouse gases, underscoring
87 the need for independent transport bias assessments to advance global carbon budget constraints.

88 To address uncertainty in ATMs for studying large-scale tracer atmospheric transport and the
89 corresponding surface fluxes, several community model intercomparison (TransCom) projects
90 have been established for various tracers including CO₂ (Baker et al., 2006; Gurney et al., 2003,
91 2004; Law et al., 2008; Patra et al., 2008), N₂O (Thompson et al., 2014), SF₆ (Denning et al.,
92 1999), SF₆ and CH₄ jointly (Patra et al., 2011), as well as an age of air tracer (Krol et al., 2018).
93 Blaine (2005) coordinated a TransCom O₂ experiment to compare model simulations of the O₂
94 seasonal cycle across the Scripps O₂ network. While this experiment provided valuable initial
95 insights into ATM performance in simulating atmospheric O₂ from ocean fluxes, substantial
96 advances in ATMs and more data collected also from aircraft and ships since then motivate an
97 updated intercomparison study with more extensive model-data comparisons and analyses. More
98 recently, CO₂ inversion intercomparisons have been coordinated through the OCO-2 MIP
99 (Crowell et al., 2019; Peiro et al., 2022; Byrne et al., 2023) and the Global Carbon Project (e.g.,
100 Friedlingstein et al., 2025). These experiments reveal substantial spread in forward tracer (e.g.,
101 CO₂) atmospheric distribution and inverted surface fluxes, driven by different ATMs and
102 inversion setups. The spread in forward transport simulations stems from multiple factors,
103 including the choice of wind fields from various reanalysis products or online simulation,
104 regridding fine resolution meteorological data to coarse model grids, the advection scheme that
105 governs large-scale mixing, and parameterized sub-grid processes, such as boundary layer
106 mixing and deep convection. Despite the complexity of different transport pathways, long-lived
107 tracers (e.g., CO₂ and O₂) at mid-latitudes tend to show tracer distributions that are aligned with
108 moist potential temperature (θ_e) surfaces. This is because θ_e surfaces are preferential surfaces for
109 mixing, leading to rapid along- θ_e mixing and slow cross- θ_e mixing (Bailey et al., 2019; Jin et al.,
110 2021; Miyazaki et al., 2008; Parazoo et al., 2011).



111 It is a critical challenge to accurately quantify the rate-limiting cross- θ_e mixing time-scales,
112 which are largely driven by diabatic processes including moist convection and radiative cooling.
113 Here, we define “diabatic mixing rates” as diffusivities that are inversely related to cross- θ_e
114 mixing time-scales. These mixing rates are important for determining the large-scale tracer
115 distribution in ATMs. Jin et al. (2024) established a framework to calculate cross- θ_e mixing rates
116 from ATMs and moist static energy (MSE) budgets from reanalysis based on a mass-indexed
117 isentropic coordinate called M_{θ_e} (Jin et al., 2021). This framework also allows cross- θ_e tracer
118 gradients from airborne observations to provide independent constraints on diabatic mixing. Jin
119 et al. (2024) tested four ATMs used in CO₂ inversions, showing that these models tend to have
120 too fast mixing in the mid-latitudes of the Southern Hemisphere in the austral summer. The too
121 fast mixing is also confirmed by the fact that models simulate smaller CO₂ gradients compared to
122 airborne observations, which is an independent constraint on the mixing rate. The mixing rate
123 constraint and CO₂ gradient constraint also have implications for biases in the inverse model
124 estimates, indicating a too large summer-time Southern Ocean (SO) CO₂ sink. This framework
125 provides a system for independently evaluating transport simulations and flux estimates.

126 Previous TransCom experiments focused primarily on tracers that only have significant sources
127 and sinks over the land, and large seasonal flux cycles tied to the northern terrestrial biosphere.
128 In contrast, APO is a tracer of surface ocean exchange with the largest seasonal variability
129 observed over mid-to-high latitude oceans in both hemispheres. APO offers a distinct perspective
130 for studying atmospheric mixing within and above the marine boundary layer, the long-range
131 tracer transport into and out of the remote Southern Hemisphere, and the ability for inverting
132 tracer flux over the SO from atmospheric measurements.

133 Here we use output from the APO-MIP1 (Stephens et al., 2025), which generated a suite of
134 forward ATM simulations of APO and its components (air-sea O₂, CO₂, and N₂ flux, and fossil
135 fuel CO₂ emission and O₂ uptake) from different source fields. This effort was initially motivated
136 by a need to support the calibration of hemispheric-scale seasonal air-sea APO flux estimates
137 from spatially and temporally sparse observations from airborne campaigns (e.g., Jin et al.,
138 2023), stations, and ships. Here we focus on the other goals of APO-MIP1 which were to use
139 atmospheric APO observations to characterize errors in ATMs and APO flux products.



In Section 3.1, we describe APO measurements from surface stations, aircraft, and ships, and the experimental design of APO-MIP1 using eight ATMs to simulate transport of three ocean APO flux products, and two fossil fuel products. In Section 3.2, we evaluate simulations against observations, revealing large model spread and errors at eastern Pacific surface stations due to mixing uncertainties, while airborne column-average data show smaller cross-ATMs variability and errors. In Section 3.3, we analyze diabatic mixing rates, demonstrating that ATMs generally overestimate mid-latitude mixing in both hemispheres, allowing us to separate transport and flux-related biases. In Section 3.4, we examine simulations of shipboard data around Drake Passage and the Antarctic Peninsula, revealing that current ATMs and flux products underestimate meridional gradients in APO seasonal amplitude from 53-65°S. The models also fail to capture the APO contrast between Palmer Station flask samples and nearby in-situ ship data due to limitations in representing local topographic flows with coarse-resolution ATMs.

2. Materials and Methods

2.1 Definition of APO

APO (per meg) is calculated from atmospheric observations of relative changes in the O_2/N_2 ratio (per meg) and CO_2 mole fraction (ppm) according to Stephens et al. (1998) as

$$APO = \delta(O_2/N_2) + \frac{1.1}{X_{O_2}}(CO_2 - 350), \quad (1)$$

with

$$\delta(O_2/N_2) = \left(\frac{(\frac{O_2}{N_2})_{sample}}{(\frac{O_2}{N_2})_{reference}} - 1 \right) \cdot 10^6. \quad (2)$$

The factor 1.1 represents the approximate exchange ratio of O_2 to CO_2 in terrestrial biospheric processes (Severinghaus, 1995). We note that this ratio generally varies from 1.01 to 1.14 in aboveground carbon pools across different temporal and spatial scales (Gallagher et al., 2017; Hockaday et al., 2009; Keeling, 1988; Worrall et al., 2013). This ratio also exhibits diurnal change and varies between respiration and photosynthesis in biosphere-atmosphere O_2 and CO_2 exchanges (Faassen et al., 2023, 2024). With our focus on seasonal variations, we use 1.1 as



representative of the O_2 to CO_2 exchange ratio during seasonal growth and decay of terrestrial biota. A sensitivity test in Jin et al. (2023) showed that varying this ratio by ± 0.05 has only minor effects on seasonal APO changes. X_{O_2} (0.2094) is the reference dry-air mole fraction of O_2 used in the definition of the O_2 scale of the Scripps O_2 Program (Keeling et al., 2020). $\delta(O_2/N_2)$ is expressed in units of per meg, while CO_2 is converted from ppm units to per meg units by subtracting a reference value of 350 ppm and then dividing by X_{O_2} . APO observations are typically expressed in per meg units, but they can be converted to ppm equivalent units by multiplying by X_{O_2} .

2.2 Atmospheric measurements

The APO-MIP1 (Stephens et al., 2025) required model output sampled to match a collection of surface station, airborne, and shipboard observations, and also accepted optional output at additional locations, at higher time resolution, and for full 3-D fields, as shown in Tables S1-2. Here we evaluate model APO simulations using observation data collected at 10 surface stations, on 10 airborne campaigns from three projects, and one repeated shipboard transect from 50 cruises. We show sampling locations, and horizontal flight and ship tracks in Fig. 1. We use surface station APO measurements (2009 to 2018) from 10 sampling sites mainly in the Pacific from the Scripps O_2 Program surface flask network (Keeling & Manning, 2014; Manning & Keeling, 2006). The airborne measurements (Stephens et al., 2021) were made on the NSF NCAR GV aircraft during the HIAPER Pole-to-Pole Observation project from 2009 to 2011 (HIPPO, Wofsy, 2011) and the O_2/N_2 Ratio and CO_2 Airborne Southern Ocean Study in 2016 (ORCAS, Stephens et al., 2018), and from the NASA DC-8 aircraft during the Atmospheric Tomography Mission from 2016-2018 (ATom, Thompson et al., 2022). Shipboard measurements were made on transects crossing the Drake Passage by the NSF ARSV Laurence M. Gould from 2012-2017 (Stephens, 2025). Details of surface station, airborne, and shipboard APO measurements are provided in Appendix A.

As the primary focus of this study is the APO seasonal cycle and its latitudinal distribution, we remove interannual trends from the observational data. For surface station and airborne measurements, we remove the long-term trend by subtracting a deseasonalized cubic spline fit



(smoothing parameter of 0.8) derived from the global mean APO time series using Scripps O₂ Program data following Hamme & Keeling (2008). For the ship data, we apply a similar detrending procedure but use only South Pole Observatory (SPO) data to derive the long-term trend.

2.3 Components of APO in the atmosphere and prescribed surface fluxes

APO exhibits seasonal variations primarily driven by air-sea exchange (F_{APO}^{ocn}), which comprises three components: air-sea exchange of O₂ ($F_{O_2}^{ocn}$), CO₂ ($F_{CO_2}^{ocn}$), and N₂ ($F_{N_2}^{ocn}$). Additionally, APO is influenced by fossil fuel emission of CO₂ ($F_{CO_2}^{ff}$) and consumption of O₂ ($F_{O_2}^{ff}$), which together combine to form a sink for APO due to fossil fuel burning (F_{APO}^{ff}). Fluxes are defined as positive to the atmosphere.

In this study, we primarily simulate APO by performing forward transport of these individual flux components in ATMs, except one inverse model flux product that provides net F_{APO}^{ocn} directly. We combined these components to calculate the net atmospheric APO anomalies in units of per meg as

$$\delta APO = \delta APO^{ocn} + \delta APO^{ff}, \quad (3)$$

with

$$\delta APO^{ocn} = \frac{1}{X_{O_2}} \cdot \Delta O_2^{ocn} - \frac{1}{X_{N_2}} \cdot \Delta N_2^{ocn} + \frac{1.1}{X_{O_2}} \cdot \Delta CO_2^{ocn}, \quad (4)$$

and

$$\delta APO^{ff} = \frac{1}{X_{O_2}} \cdot \Delta O_2^{ff} + \frac{1.1}{X_{O_2}} \cdot \Delta CO_2^{ff}. \quad (5)$$



210 where ΔO_2^{ocn} , ΔN_2^{ocn} , ΔCO_2^{ocn} , ΔO_2^{ff} , and ΔCO_2^{ff} represents the atmospheric fields in units of
211 deviations in ppm of each flux component ($F_{O_2}^{ocn}$, $F_{CO_2}^{ocn}$, $F_{N_2}^{ocn}$, $F_{O_2}^{ff}$, and $F_{CO_2}^{ff}$) that is forward
212 transport in the ATMs (Stephens et al., 1998). The δ sign denotes tracers in units of per meg.

213 We utilize three distinct ocean APO flux products: (1) the Jena product, which directly provides
214 F_{APO}^{ocn} from an atmospheric APO inversion framework that assimilates surface station
215 measurements (Rödenbeck et al., 2008); 2) the CESM product, an Earth System Model
216 simulation with prognostic ocean biogeochemistry (Yeager et al., 2022; Long et al., 2021) that
217 generates separate flux components ($F_{O_2}^{ocn}$ and $F_{CO_2}^{ocn}$); and 3) the DISS product, which provides
218 separate observation-based flux components incorporates surface ocean dissolved oxygen
219 measurements (Garcia & Keeling, 2001; Resplandy et al., 2016) and pCO₂ data (Jersild et al.,
220 2017; Landschützer et al., 2016). $F_{N_2}^{ocn}$ for CESM and DISS is estimated by scaling ocean heat
221 fluxes from CESM and ERA-5, respectively, using the relationship of Keeling et al. (1993). For
222 fossil fuel contributions, we employ the OCO2MIP product for CO₂ emissions (Basu & Nassar,
223 2021) and the GridFED database for coupled O₂ and CO₂ fluxes from fossil fuel combustion
224 (Jones et al., 2021). Details of each product are provided in Appendix B. All flux fields were
225 linearly interpolated from their original temporal and spatial resolution to 1° longitude × 1°
226 latitude with daily temporal resolution from 1986 to 2020. When flux data were unavailable in
227 the earlier portion of this time period (Jena and OCO2MIP), we set the corresponding fluxes to
228 zero. Participating modelers were requested to simulate at least from 2009 to 2018, following
229 three years of spin up from 2006 to 2008, and optionally longer (Table 1). In addition to Jena,
230 which is simulated directly, we construct the two ΔAPO^{ocn} products using Eq. 4 and two ΔAPO^{ff}
231 products using Eq. 5, as described in Appendix B. Fig. 2 illustrates the seasonal and latitudinal
232 flux patterns of these three ocean APO flux products and the fossil fuel APO flux from GridFed,
233 which serves as our primary fossil fuel flux dataset in this study.

234 2.4 Atmospheric tracer transport models

235 We simulate each component of APO in the atmosphere using the flux fields described in Section
236 2.3, and eight ATMs (see Table 1). All tracer atmospheric fields are modeled as tracer deviations



237 against an arbitrary background with concentrations in ppm dry air mole fraction (as for CO₂).
238 These tracer mole fractions are later converted to deviations in units of per meg after subtracting
239 the model-specific arbitrary reference according to Eq. 4. We describe key model parameters and
240 setups below.

241 2.4.1 CAM-SD

242 The Community Atmosphere Model (CAM) version 6.0 is the atmospheric component of
243 CESM2 (Danabasoglu et al., 2020). The version used here is run online with specified dynamics
244 (SD), wherein the model is constrained with MERRA-2 reanalysis, and uncoupled from the other
245 climate system components. Temperature and horizontal winds (u and v) are nudged to
246 MERRA-2, 8 times per day, with a normalized strength coefficient of 0.25. Shallow convection
247 is parameterized following the Cloud-Layers Unified by Binormals framework (CLUBB, Golaz
248 et al., 2002), and deep convection is parameterized following Zhang & McFarlane (1995). CAM
249 has not been used for tracer inversions, but has been evaluated extensively for its dynamical
250 properties (e.g., Bailey et al., 2019; Kay et al., 2012)

251 2.4.2 CAMS_LMDZ

252 CAMS_LMDZ refers here to the offline transport model from the Atmospheric General
253 Circulation Model of Laboratoire de Météorologie Dynamique, called LMDz. LMDz is the
254 atmospheric component of the Earth System Model of Institut Pierre-Simon-Laplace (IPSL). It is
255 also used to drive the offline model CAMS_LMDz, in which case its horizontal winds are
256 nudged to those of the ERA5 reanalysis. From the computer code of LMDz, CAMS-LMDz only
257 keeps the transport subroutines for advection (Hourdin & Armengaud, 1999), deep convection
258 (Emanuel, 1991), thermals (Rio & Hourdin, 2008), and boundary-layer turbulence (Hourdin et
259 al., 2006). All other processes are replaced by an archive of relevant meteorological variables
260 (air mass fluxes, exchange coefficients, temperature, etc.) built with the full LMDz model at the
261 target spatial resolution, thereby allowing relatively small computing time and resources for the
262 offline model. LMDz ensures the physical consistency of the archive of meteorological variables.
263 The meteorological variables are stored as 3-hourly averages. CAMS_LMDZ has been regularly
264 participating in OCO-2 MIP (Byrne et al., 2023) and TransCom intercomparison studies.



265 2.4.3 CTE_TM5

266 TM5 is a tracer transport model used for simulating atmospheric trace gas chemistry and
267 transport (Krol et al., 2005). We refer to it as CTE_TM5 because the model was run with the
268 CarbonTracker-Europe (CTE) shell, but this does not alter the TM5 physics and chemistry. TM5
269 advection is computed using the slopes advection scheme (Russell & Lerner, 1981) and in this
270 work it is driven by ERA-5 reanalysis wind fields (Hersbach et al., 2020), making it an offline
271 model. The convection is computed from the convective entrainment and detrainment fluxes
272 from the ERA-5 reanalysis. Free tropospheric diffusion is computed using the formulation by
273 Louis (1979). Diffusion in the boundary layer is computed using the parametrization by Holtslag
274 & Boville (1993), where the diurnal variability in the boundary layer height is computed using
275 Vogelesang and Holtslag (1996). TM5 is widely used in inversions and regularly participates in
276 MIPs, for different tracers at different model resolutions and driven with different wind
277 reanalysis products (for example, Byrne et al., 2023; Friedlingstein et al., 2025; Gaubert et al.,
278 2019; Krol et al., 2018).

279 2.4.4 TM3

280 TM3 (Heimann & Körner, 2003) is an offline atmospheric tracer transport model, in the present
281 runs driven by meteorological fields from the NCEP reanalysis (Kalnay et al., 1996). It was run
282 here on a spatial resolution of 5 degrees longitude, about 3.8 degrees latitude, and 19 vertical
283 layers. The advection uses the slopes scheme (Russell & Lerner, 1981), which is the same as in
284 TM5. Boundary layer mixing is parameterized according to Louis (1979). Vertical mixing due to
285 sub-grid-scale cumulus clouds is calculated using the mass flux scheme of Tiedke (1989). TM3 is
286 the ATM used in Jena APO inversion (Rödenbeck et al., 2008), which is one of the flux products
287 used in this study.

288 2.4.5 MIROC4-ACTM

289 MIROC4-ACTM is a new generation Model for Interdisciplinary Research on Climate (MIROC,
290 version 4.0; Watanabe et al., 2008) atmospheric general circulation model (AGCM)-based
291 chemistry-transport model (ACTM; Patra et al., 2018). This AGCM is evolved from the Center
292 for Climate System Research, University of Tokyo (CCSR) / National Institute for



293 Environmental Studies (NIES) / Frontier Research Center for Global Change, JAMSTEC
294 (FRCGC) AGCM version 5.7b (Numaguti et al., 1997). The MIROC4 AGCM propagates only
295 explicitly resolved gravity waves into the stratosphere through the implementation of a hybrid
296 vertical coordinate system compared to its predecessor AGCM5.7b. The MIROC4 AGCM
297 online-simulated horizontal winds and temperature are nudged to the Japanese 55-year
298 Reanalysis (JRA-55) at 6-hourly time intervals (Kobayashi et al., 2015). MIROC4-ACTM
299 produces “age-of-air” up to about 5 years in the tropical upper stratosphere (~1 hPa) and about 6
300 years in the polar middle stratosphere (~10 hPa), in agreement with observational estimates. The
301 convective transport and inter-hemispheric transport of tracers in the model are validated using
302 ²²²Radon and sulphur hexafluoride (SF₆), respectively (Patra et al., 2018).

303 2.4.6 NICAM-TM_gl5 and NICAM-TM_gl6

304 NICAM-TM is an atmospheric transport model based on the Nonhydrostatic Icosahedral
305 Atmospheric Model (NICAM) (Niwa et al., 2011; Satoh et al., 2014). In this study, we used the
306 offline mode of NICAM-TM, which uses air mass fluxes, vertical diffusion coefficients and
307 other meteorological variables; those data are calculated in advance by an online calculation of
308 NICAM, in which horizontal winds are nudged toward the JRA-55 data. In NICAM, the air mass
309 fluxes are calculated consistently with the continuity equation while conserving tracer masses,
310 which do not require any numerical mass fixing (Niwa et al., 2011). For APO-MIP1, two
311 horizontal resolutions were used: “glevel-5” (gl5) and “glevel-6” (gl6), whose mean grid
312 intervals are 223 and 112 km, respectively. The number of the vertical model layers is 40 and the
313 top of the model domain is at approximately 45 km. The vertical diffusion coefficients are
314 calculated with the MYNN (Mellor & Yamada, 1974; Nakanishi & Niino, 2004) Level 2 scheme
315 (Noda et al., 2010). The cumulus parameterization scheme used in NICAM-TM is Chikira &
316 Sugiyama (2010). Model performance for atmospheric constituent transport can be found in
317 Niwa et al. (2011, 2012).

318 2.4.7 NIES

319 NIES-TM-FLEXPART is a coupled transport model combining Eulerian (NIES-TM) and
320 Lagrangian (FLEXPART) models. It is a transport modeling component of the variational flux



inverse modeling system NIES-TM-FLEXPART-Variational (NTFVAR, Maksyutov et al., 2021). The NIES Transport Model (NIES-TM) is an offline model, originally developed in the 1990s (Maksyutov et al., 2008). In this study, the NIES-TM v.21 is used, which improves SF₆ transport and tropopause height over the former v.08.1 (Belikov et al., 2013), as evaluated in Krol et al. (2018), due to (a) using ERA5 hourly wind data, including vertical wind on model coordinates, on 137 model levels and a 0.625° grid for preparation of the 4-hourly average mass fluxes on 42 hybrid-pressure levels, (b) transporting first-order moments (Russell & Lerner, 1981; Van Leer, 1977) for advection, (c) applying penetrative convection rate and turbulent diffusivity supplied by the ERA5 reanalysis (Hersbach et al., 2020). The version v.21 is the same as used in the OCO-2 MIP (Byrne et al., 2023). NIES-TM is coupled with the Lagrangian model FLEXPART (Stohl et al., 2005) to provide refinement to the near field transport during the last 3 days prior to the observation event as presented by (Belikov et al., 2016). FLEXPART model v.8.0 is driven by 6-hourly JRA-55 winds, interpolated to 40 hybrid pressure levels and 1.25°x1.25° resolution. The surface flux footprints are produced by FLEXPART at 1°x1° resolution and daily time step.

Table 1. Participating ATMs and model parameters.

Abbreviation	Model System	Grid (latitude × longitude × levels)	Meteorology	Run start, valid period	Reference(s)
CAM-SD	Community Atmospheric Model	0.9° × 1.25° × 56	MERRA-2	1986, 1989-2019	Danabasoglu et al., 2020
CAMS_LMDZ	Copernicus Atmosphere Monitoring Service	1.875° × 3.75° × 39	ERA5	1986, 1991-2020	Chevallier, 2013; Chevallier et al., 2005, 2010
CTE_TM5	CarbonTracker Europe	1° × 1° × 25	ERA5	2000, 2003-2020	Luijkx et al., 2017



Jena_TM3	TM3	$4^{\circ} \times 5^{\circ} \times 19$	NCEP	1986, 1989-2020	Heimann & Körner, 2003
MIROC4- ACTM	MIROC4- ACTM	$2.8^{\circ} \times 2.8^{\circ} \times 67$	JRA-55	1986, 1991-2020	Chandra et al., 2022; Patra et al., 2018
NICAM- TM_g15	NICAM-based Transport Model	$\sim 223 \text{ km} \times 40$	JRA-55	1986, 1989-2020	Niwa et al., 2011, 2017
NICAM- TM_g16		$\sim 112 \text{ km} \times 40$			
NIES	NIES-TM- FLEXPART	$3.75^{\circ} \times 3.75^{\circ} \times 42$ (NIES-TM); $1^{\circ} \times 1^{\circ} \times$ 40 (FLEXPART)	JRA-55	2000, 2003-2020	Belikov et al., 2016; Maksyutov et al., 2021

336 2.5 Outputs from transport models

337 For each ATM, we required simulations for all species sampled to match with the observation
338 locations and times in a subset of the full ObsPack CO₂ files GLOBALVIEWplus v7.0 ObsPack
339 (Schuldt et al., 2021) , excluding the model spin-up period. This subset corresponds to existing
340 APO observations that are analyzed in this study from Scripps O₂ Program surface stations, NSF
341 NCAR airborne observations, and NSF NCAR and AIST/JMA shipboard programs. The full list
342 of these records is in Table S1. We note that, while the HIPPO, ORCAS, ATom, and Gould
343 ObsPack files contain CO₂ observations from different instruments, their 10-sec sampling times
344 align with the NSF NCAR APO measurements, except during calibration periods for either
345 instrument.

346 We also received optional output, which includes the full set of ObsPack files, 3-D atmospheric
347 fields, meteorological variables, additional ship data, and output at additional fixed sites (Table
348 S2). Further details are provided in the APO-MIP1 protocol available at Stephens et al. (2025).
349 We obtained output matching the full set of ObsPack files from four ATMs, which will be useful
350 for future network design. We obtained daily mean 3-D gridded concentration fields from six



ATMs. These fields support the calculation of diabatic mixing rates, which we use to evaluate ATMs and the flux products, following the method of Jin et al. (2024). Details are in Section 3.2. We also received hourly (from two versions of NICAM) or 3-hourly (from NIES) output for an extensive list of sites with past or ongoing APO measurements, and co-located samples for ship sampling programs of NIES VOS, AIST R/V Mirai, and UEA Cap San Lorenzo (Hamburg Süd) from three models. These data are not analyzed in this study, but are made available at Stephens et al. (2025).

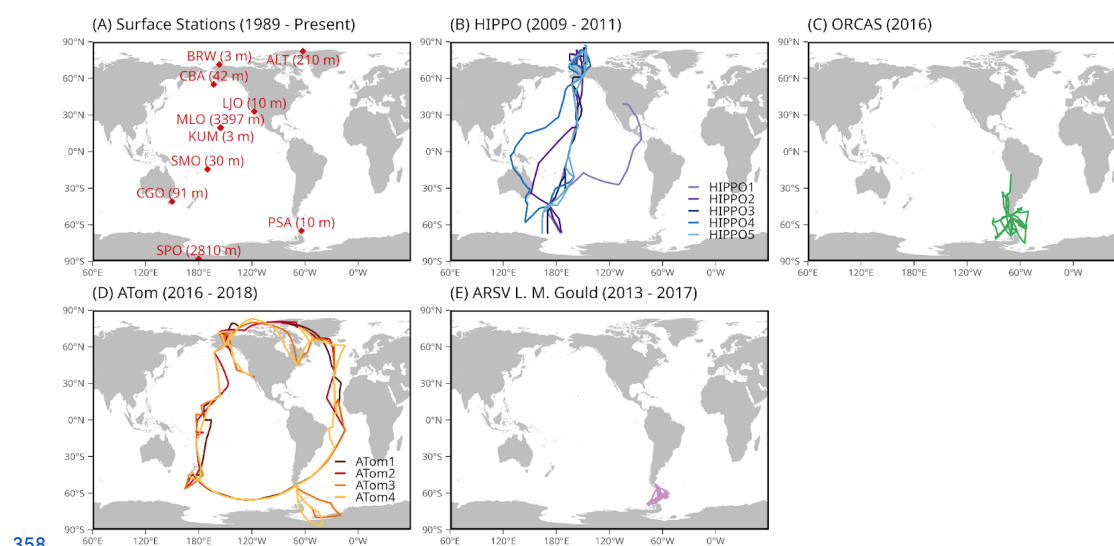
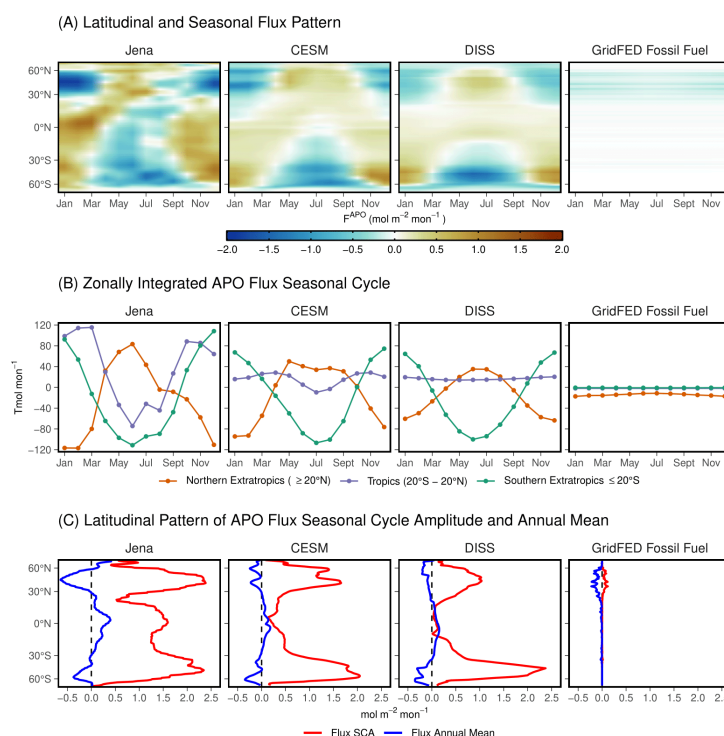


Figure 1: Geographic distribution of APO observations used in this study: (A) Scripps O₂ Program surface stations (red diamonds) with station codes and inlet elevation in meters above sea level; (B) HIPPO (1 to 5) airborne campaign horizontal flight tracks covering the Pacific Ocean; (C) ORCAS aircraft measurements concentrated in the Drake passage; (D) ATom (1 to 4) airborne campaign horizontal flight tracks covering the Pacific and Atlantic Oceans; and (E) Ship-based measurements from the RV *Laurence M. Gould* operating in the Drake passage.



365

366 Figure 2: Comparison of APO flux patterns from the three air-sea flux products (Jena, CESM,
367 and DISS) and fossil fuel emissions (GridFed), averaged from 2009 to 2018. (a) Hovmöller
368 diagrams showing the spatiotemporal distribution of APO fluxes ($\text{mol m}^{-2} \text{mon}^{-1}$) as a function of
369 latitude and month. (b) Seasonal cycles of zonally integrated fluxes for three latitude bands:
370 Northern Extratropics ($\geq 20^\circ\text{N}$, orange), Tropics ($20^\circ\text{S} - 20^\circ\text{N}$, lavender), and Southern
371 Extratropics ($< 20^\circ\text{S}$, green). (c) Latitudinal profiles of flux seasonal cycle amplitude (SCA, red)
372 and annual mean flux (blue). For the annual mean profiles (blue lines in panel C), only the
373 latitudinal gradients should be interpreted, as the global means may contain biases in the ocean
374 flux products, which are not the focus of this paper.



375 **3. Results and discussion**

376 **3.1 APO model-observation comparisons at surface stations and along aircraft** 377 **flight tracks**

378 **3.1.1 APO seasonal and latitudinal variations at surface stations**

379 We show observations and model simulations of APO seasonal cycles at 10 surface stations of
380 the Scripps O₂ program network in Fig. 3. We present annual mean values, seasonal cycle
381 amplitudes (SCA), and phase from both observations and model simulations at these surface
382 stations in Fig. 4, with model errors shown as colors. Observations show clear meridional
383 gradients in APO annual means (Fig. 4A), with higher values in the Southern Hemisphere than
384 Northern Hemisphere, and a southern tropical “bulge” (Battle et al., 2006; Gruber et al., 2001;
385 Stephens et al., 1998). The APO SCA shows higher values in the high latitudes of both
386 hemispheres, with larger amplitudes in the Southern Hemisphere compared to the Northern
387 Hemisphere, yet reaches its maximum at the northern mid-latitude station Cold Bay (CBA) (Fig.
388 4B). The seasonal phase exhibits an approximately 6-month difference between hemispheres,
389 while remaining relatively uniform within each hemisphere (Fig. 4C).

390 The higher annual mean APO in the Southern Hemisphere and the southern tropical “bulge” is a
391 result of southward O₂ and CO₂ transport by the oceans, further amplified by net APO uptake in
392 the Northern Hemisphere from fossil fuel burning (Keeling & Manning, 2014; Stephens et al.,
393 1998). The larger APO SCA in mid- to high-latitudes reflects more pronounced seasonal flux
394 cycles resulting from larger marine net primary production (NPP) and sea surface temperature
395 changes in these regions. The thermal and biological effects on APO SCA are further enhanced
396 at eastern Pacific coastal sites (e.g., LJO and CBA), where the shallow marine boundary layer
397 traps high-APO air masses during summer. The 180-days phase difference between the two
398 hemispheres is a result of different seasonal heating and cooling, as well as the biological cycle.

399 **3.1.2 Biases in APO-MIP1 simulations at surface stations**

400 APO-MIP1 simulations of APO annual means and seasonal cycles at surface stations broadly
401 agree with observations (Figs. 3-4). Simulations driven by CESM fluxes show the best



agreement with observed APO features. For annual mean spatial patterns (Fig. 4A), CESM- and DISS-driven simulations show comparable performance in representing the southern tropical “bulge” and north-south gradient in annual means, while significantly outperforming simulations using the Jena flux model in northern stations. The main limitation of simulations using CESM fluxes is an overestimation of annual mean APO values across Pacific sites in the Southern Hemisphere, and an underestimation at LJO. Simulations using DISS fluxes also underestimate the annual mean APO at LJO.

APO SCA is well represented in simulations driven by CESM flux, but the SCA at LJO is significantly underestimated in all ATMs except CAM-SD. The underestimation is caused by an overly weak summer-time APO peak (Fig. 3), which also leads to the small annual mean presented above. Simulations using DISS flux generally underestimate SCA, especially in the high latitudes. Simulations using Jena flux, however, generally overestimate the SCA in the mid- to high-latitudes. We find largest SCA biases and cross-ATMs spread at LJO and CBA when using the Jena flux. The biases and model spread are closely related to underrepresentation in ATMs, and will be discussed in the next section. We note that the model biases and spread observed at surface stations are smaller than those reported in the previous TransCom-O₂ experiment (Blaine, 2005), indicating improved atmospheric transport modeling.

Phase simulations using CESM flux are consistent with observations at most stations, except at two northern low-latitude stations, KUM and MLO, where we find too late seasonal minimum day by up to two weeks. Simulations using DISS flux show even larger biases, with earlier seasonal minimum days at all southern and northern low-latitude stations.

3.1.3 Impact of ATM mixing biases

We find APO-MIP1 simulations have large model spread and biases at two northern mid-latitudes stations, LJO and CBA (Fig. 3), especially simulations using Jena fluxes. We note that the interdependence of transport models and fluxes in inversions can be seen for the Jena flux product simulations at LJO (Figs. 3-4). As expected, we see good agreement with observations for the Jena flux product transported by the same model used in the Jena APO inversion (Jena_TM3). However, all other ATMs overestimate summertime APO, and consequently SCA, for the Jena flux product at LJO, CBA, and BRW. All other ATMs also



431 simulate too negative wintertime APO at LJO. These biases suggest a stronger regional APO
432 source in the Jena flux product that could have resulted from too rapid dilution of surface flux
433 signals at LJO in both summer and winter.

434 Surface station simulations using CESM flux (Figs. 3-4) also reveal elevated model spread and
435 observation deviations at LJO and CBA. At LJO, all ATMs underestimate summertime APO, and
436 consequently SCA, implying too weak upwind outgassing fluxes. The relative magnitude of
437 simulated summer-time peaks for CESM at LJO and CBA maintains a consistent pattern across
438 different flux products, with CAM-SD consistently showing the highest values and Jena_TM3
439 the lowest, regardless of the flux product used, suggesting consistent biases in the ATMs.

440 This substantial cross-ATMs variability highlights the challenges in accurately representing
441 complex atmospheric vertical transport processes in regions where strong temperature inversions
442 and stratocumulus clouds significantly influence vertical mixing (Naegler et al., 2007; Nevison et
443 al., 2008). The Jena flux product, derived from an inversion that assimilates these station data,
444 relies on the TM3 tracer transport model (Rödenbeck et al., 2008). Previous studies indicate that
445 TM3 consistently overestimates vertical mixing over the Eastern Pacific, leading to larger
446 inverted seasonal fluxes to match station observations (Jin et al., 2023; Naegler et al., 2007). Our
447 analysis suggests that in comparison to Jena_TM3, vertical mixing is weaker in the two versions
448 of NICAM, CAM-SD, MIROC4-ACTM, and CTE_TM5, which show larger summer-time APO
449 anomalies at LJO and CBA. This pattern is consistent across the three flux products considered.

450 The larger model spread at northern coastal sites (e.g., LJO, CBA, and BRW) also highlights the
451 limitations of current coarse-resolution ATMs in representing horizontal coastal flows and
452 land-sea breezes. At LJO, samples are collected only during steady west wind (from the ocean)
453 conditions (Keeling et al., 1998). However, ATMs failed to capture the actual small-scale
454 atmospheric conditions associated with on-shore winds during episodic storm systems, which
455 leads to significant underestimation of oceanic influence (Keeling et al., 1998). APO, as a tracer
456 of air-sea gas exchange, is particularly sensitive to the dilution effects in coarse-resolution
457 models.



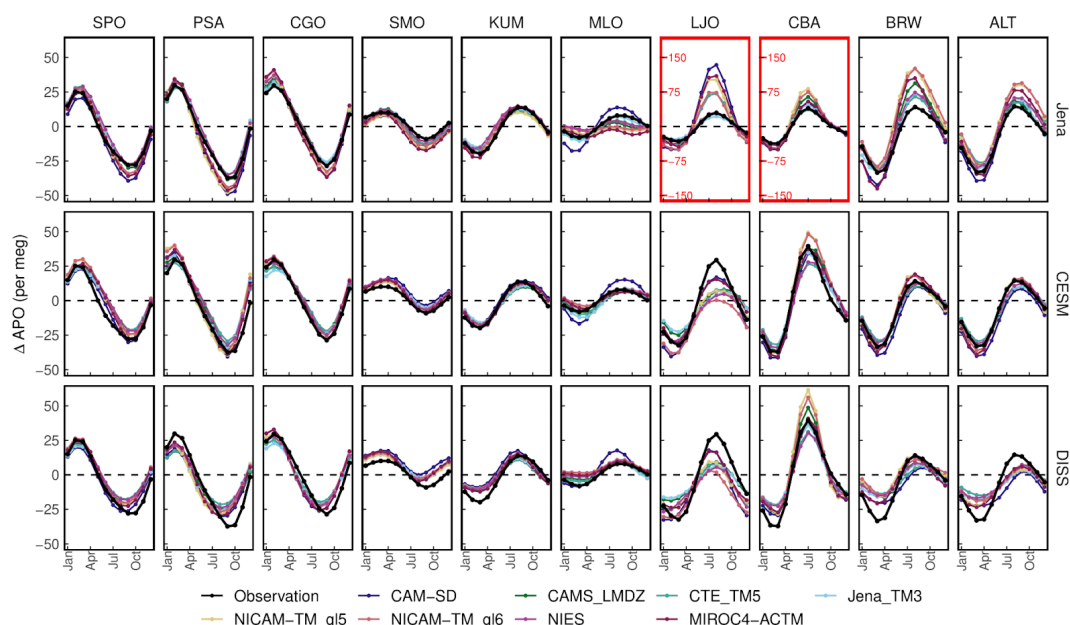
3.1.4 APO seasonal and latitudinal variations along flight tracks and biases in APO-MIP1

We present zonal averages of APO annual means, SCA, and seasonal minimum days derived from airborne data, grouped into 10-degree latitude and 100-mbar bands in Fig. 5A-C (full seasonal cycles in Fig. S1). We further calculate these three metrics as column-average (black) and at 900-mbar (blue) in Fig. 5D-F, where we also compare them with surface station data (shown as red points). The airborne data show patterns similar to those seen at surface stations but provide detailed vertical structures. The vertical profiles consistently show larger SCA at low altitudes, indicating that the main drivers of SCA are near the surface, while annual means and seasonal phases remain uniform across altitudes. Airborne column averages show increasing SCA and decreasing annual means from low to high latitudes, with similar SCA and annual mean values north of 50°N (Fig. 5D-E), whereas station observations show peaks in the mid-latitudes (LJO and CBA) due to high-APO air masses being trapped below the summer marine boundary layer. This trapping effect is also evident in airborne data interpolated to 900-mbar.

We also calculate APO annual means, SCA, and phases using aircraft simulations from APO-MIP1 (full seasonal cycles in Fig. S1) and compare simulated and observed column averages (1000-400 mbar average) in Fig. 6, with biases in column averages and vertical profiles shown in Figs. S2 and S3-5, respectively. Airborne observation-model comparisons complement those using surface station data. We find similar model biases to those seen in surface data, for example, larger SCA at northern high latitudes with the Jena flux product and smaller SCA at high latitudes with the DISS flux product. The airborne data also reveal three key biases that are not resolved at surface stations. Observations suggest a consistent near-zero annual mean APO in the Southern Hemisphere (south of 30°S), with a spike between 40° and 50°S. However, all three flux products show gradually decreasing annual mean APO south of 30°S, with CESM and DISS flux products showing a smaller spike in magnitude between 40° and 50°S. Simulations using CESM and DISS flux products show a larger SCA in the northern mid-latitudes (40 - 60°N). Additionally, simulations using the Jena flux product in the low northern latitudes show a seasonal minimum day similar to the Southern Hemisphere phase. This bias is caused by low-latitude flux features in the Jena inversion that largely replicate the Southern Hemisphere cycle, likely due to limited observational constraints in this region (Jin et al., 2023).

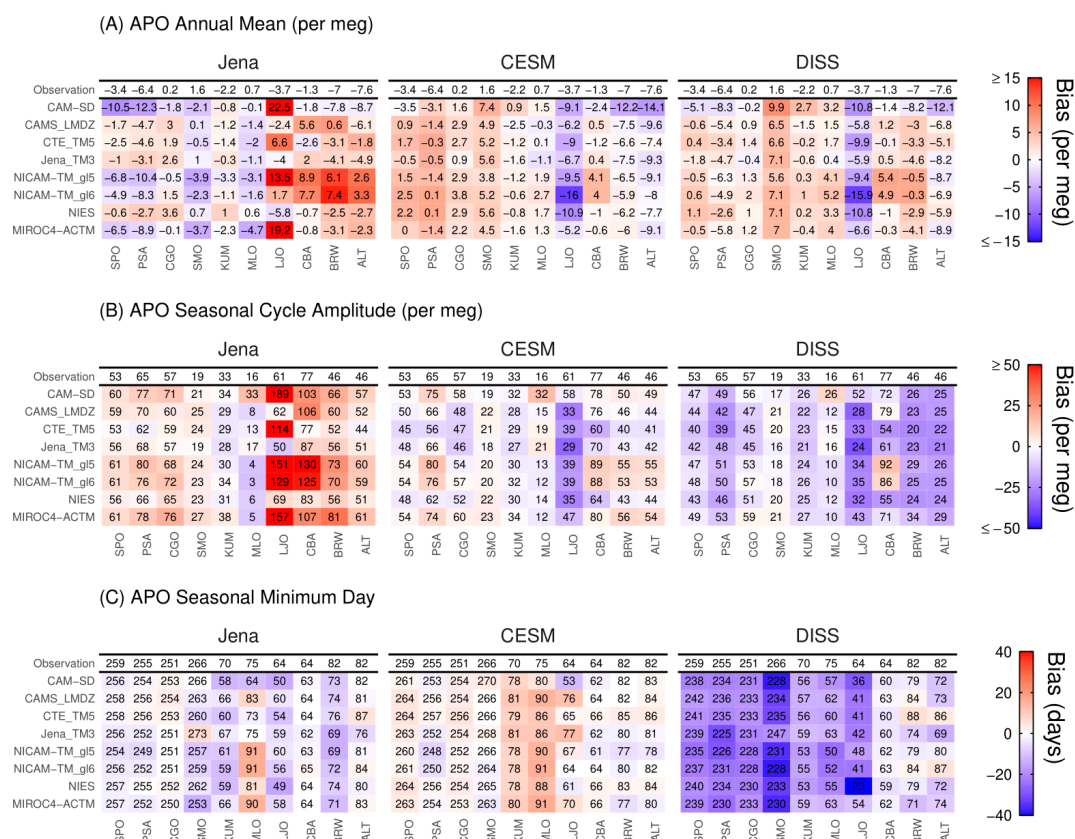


488 Our analysis demonstrates that global airborne measurements provide distinct advantages over
489 station data for evaluating large-scale flux patterns due to the reduced sensitivity of column
490 averages to boundary-layer ATM transport uncertainties. While surface stations show substantial
491 cross-model spread in simulated APO (Figs. 3-4), column-averaged airborne simulations (Fig. 6)
492 reveal remarkable consistency across ATMs when driven by the same flux product. This
493 consistency suggests that column-averaged measurements effectively integrate over local
494 transport features that often dominate surface observations. Here we establish CESM as the most
495 realistic flux product among the three products. The better agreement between observations and
496 CESM-driven simulations provides a more reliable baseline for isolating and quantifying
497 transport-related discrepancies in individual ATMs.



498

499 Figure 3: Comparison of simulated and observed APO seasonal cycles at 10 surface stations
500 (Fig. 1A), organized from southern high-latitudes (left) to northern high-latitudes (right). In each
501 panel, the black line represents observations, while colored lines show simulations from different
502 transport models. Each row of panels corresponds to the three different flux products (Jena,
503 CESM, and DISS). In each panel, the y-axis shows APO anomalies in per meg units, and the
504 x-axis shows months from January to December. We note that, for LJO and CBA simulations
505 using the Jena fluxes, a different y-axis range (three times larger) is used compared to the other
506 panels. Observations and model simulations at each station are first detrended using a
507 multiple-station weighted average trend. We calculate monthly mean seasonal APO from 2009 to
508 2018 for both observations and model simulations.



509

510 Figure 4: Evaluation of APO (A) annual mean relative to a multi-station global mean, (B)

511 seasonal cycle amplitude, and (C) seasonal minimum day across surface stations using different

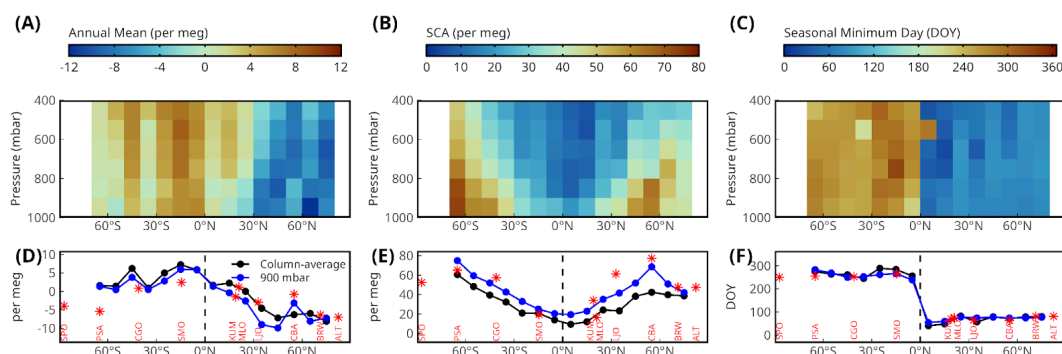
512 flux-transport model combinations. For each panel, results are organized by flux products

513 (JENA, CESM, DISS) in columns and transport models in rows, with observations on the top.

514 The metrics are printed in black, with background colors indicating biases relative to

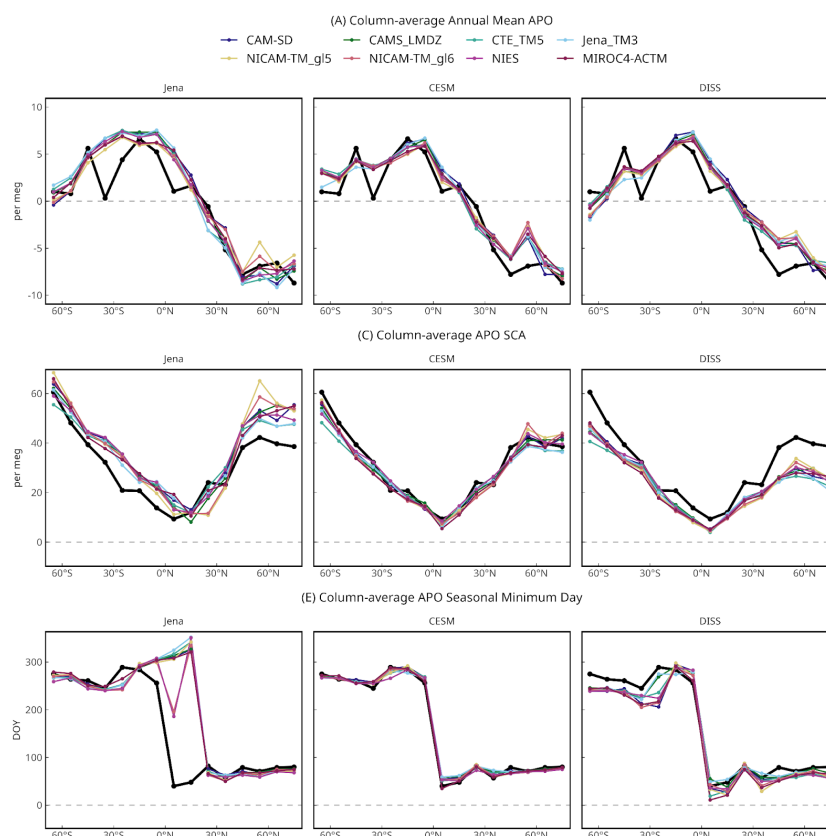
515 observations. Positive bias is shown in red, and negative bias is shown in blue.

516



517

518 Figure 5: APO annual means (A and D), SCA (B and E), and seasonal minimum day (C and F)
 519 derived from airborne observations. In A-C, we show latitude-pressure distributions, with data
 520 binned into 10 deg latitude by 100-mbar pressure boxes. In D-F, we show 1000-400 mbar
 521 column-averaged (black) and 900-mbar interpolated (blue) values, and also surface station
 522 observations (2009 to 2018). Annual mean is derived from a two-harmonic fit with constant
 523 offset, where the global multi-station trend has been subtracted to detrend the airborne
 524 observations and center the values around zero globally. SCA is calculated as the peak-to-trough
 525 amplitude of the two-harmonic fit, and seasonal minimum day is calculated as the day of
 526 seasonal trough of the two-harmonic fit.



527

528 Figure 6: Comparison of column-average (1000-400 mbar) APO features across latitude from
529 aircraft observations and model simulations using three different flux products (Jena, CESM, and
530 DISS). The figure is organized into three sets of panels showing (A) annual mean APO relative
531 to a multi-station global mean, (B) SCA, and (C) seasonal minimum day. For each feature, we
532 show latitudinal distributions of observations (black lines) and model simulations (colored lines).
533 We note that the global mean value has been subtracted from the annual mean values (A) at each
534 latitude to highlight spatial patterns. We show the column-average (400-1000 mbar) seasonal
535 cycles of observed and simulated APO for each 10° latitude band in Fig. S1.

536 3.2. Evaluation of diabatic mixing rates diagnosed from transport models

537 In this section, we evaluate the mixing timescale across mid-latitude moist isentropes of each
538 ATM using the framework developed in Jin et al. (2024). This framework was applied to identify



biases in four ATMs in the mid-latitude Southern Hemisphere using two independent constraints: (1) diagnosed diabatic mixing rates, and (2) cross-isentrope CO_2 gradients. Here we extend the framework to use APO gradients, to include two more reanalysis products, and the analysis in the Northern Hemisphere. We evaluate six of the eight ATMs participating in APO-MIP1 that provide 3-D atmospheric fields (CAM-SD, CTE_TM5, Jena_TM3, NICAM-TM_gl5, NICAM-TM_gl6, and MIROC4-ACTM), which are required to diagnose diabatic mixing rates. Diabatic mixing rates and APO gradients are diagnosed based on the mass-indexed isentropic coordinate M_{θ_e} , which was first introduced by Jin et al. (2021). For each pair of transport models and flux products, we resolve cross- M_{θ_e} diabatic mixing rates and cross- M_{θ_e} APO gradients in the mid-latitudes of both hemispheres. We use observation-based diabatic mixing constraints diagnosed from four meteorological reanalyses, and observed APO gradient constraints calculated from three airborne campaigns. The detailed methodology for calculating M_{θ_e} surfaces, diabatic mixing rates, and cross- M_{θ_e} APO gradients is provided in Appendix C.

We show the climatological monthly mean diabatic mixing rates of two M_{θ_e} surfaces in the Southern Hemisphere in Fig. 7, as well as schematics of the geographic distribution of the two M_{θ_e} surfaces. For each ATM, mixing rates in Fig. 7 are calculated from APO and averaged over three realizations diagnosed from using three flux products. The reanalysis mixing rates are calculated from moist static energy (MSE) budget and shown as average and 1σ spread over the four reanalysis products. The six ATMs and the reanalyses show diabatic mixing rates with clear seasonal cycles, suggesting more rapid mixing across isentropes in the austral winter than summer. ATMs generally overestimate diabatic mixing rates, especially in the summer and winter, when there are large cross- M_{θ_e} APO gradients that lead to well-defined mixing rates. Among the six ATMs, CTE_TM5 and Jena_TM3 show too rapid mixing that is biased high in all seasons. The other four ATMs align better with reanalysis, but still show significant overestimation for most of the year. MIROC4-ACTM shows the best performance. These findings align with Jin et al. (2024), which previously identified that the southern hemisphere summer-time mixing rates are overestimated in ATMs used for CO_2 inversions, with consistent results for the three ATMs (MIROC4-ACTM, Jena_TM3, and CTE_TM5) being used in both studies.



We find that biases in diagnosed diabatic mixing rates correlate with biases in cross- M_{0e} APO gradients in each season, with stronger diabatic mixing leading to smaller APO gradients (Fig. 8). Fig. 8 shows the ATM-diagnosed diabatic mixing rates and simulated APO gradients (points) across six transport models and three flux products at two M_{0e} surfaces (30 and 45×10^{16} kg M_{0e}) for three selected 2-month periods in the Southern Hemisphere. The points suggest clear linear relationships between diagnosed mixing rates and simulated APO gradients for each flux product (shown as fit lines for each flux product). The linear relationships persist across all seasons and M_{0e} surfaces, though with varying slopes depending on the underlying fluxes (Fig. 8). ATMs generally underestimate cross- M_{0e} absolute APO gradients (i.e., a closer to zero gradient) at both M_{0e} surfaces, corresponding to the overestimation of diabatic mixing rates in these models. For each flux product, biases in cross- M_{0e} APO gradients are always larger in fast mixing ATMs (e.g., Jena_TM3 and CTE_TM5) compared to slow mixing ATMs (e.g., two versions of NICAM-TM, MIROC4-ACTM, and CAM-SD), with MIROC4-ACTM showing the best agreement. For each transport model, the simulated gradient shows clear spread across different flux products. The largest spread occurs in austral winter and spring (Fig. 8C-D), when simulations with the DISS fluxes show much larger gradients compared to CESM or Jena fluxes. We note that the direct comparison of simulated and observed gradients for individual models is complicated by the interplay of ATM biases and flux product biases.

To evaluate flux products independently of transport model biases, we leverage both diabatic mixing rates and APO gradients. For each flux product, the intersection between the mixing rate-gradient linear fit and the MSE-diagnosed mixing rate indicates the expected APO gradient with realistic mixing characteristics. Therefore, we can evaluate large-scale flux features in the flux products by comparing this expected gradient to the observed gradient. Our analysis in Fig. 8 suggests that CESM is the most realistic flux product in the mid-latitude Southern Hemisphere in all seasons. The expected CESM gradients (intersections of thin blue line and vertical gray band) fall within the observation uncertainty range in all seasons and surfaces except austral summer at the 30×10^{16} kg M_{0e} surface (Fig. 8A), which suggests a slight underestimation of uptake in the CESM product. The expected gradients of the Jena flux product also generally fall within the observation uncertainty range, but shows an even larger underestimation in Fig. 8A. The expected gradients of the DISS flux product have large biases in the mid-latitude Southern Hemisphere. The expected gradient is significantly larger in the austral winter (Fig. 8C-D), and



significantly smaller at the 30×10^{16} kg M_{0e} surface in austral summer (Fig. 8A) and austral spring (Fig. 8E), suggesting seasonal biases in the flux pattern.

Biases in expected gradients relative to observed gradients result from errors in the magnitude and spatial distribution of air-sea APO flux, specifically the difference in flux magnitudes between regions north and south of the target M_{0e} surface. For instance, a positive expected gradient bias during austral summer at the 30×10^{16} kg M_{0e} surface (Fig. 8A) in the DISS product could stem from underestimated outgassing in high southern latitudes, excessive outgassing in lower latitudes, or both. In addition, a flux product could produce realistic expected gradients despite underestimating absolute fluxes both north and south of the M_{0e} surface if the difference remains correct. Resolving these inherent ambiguities requires additional observational constraints from surface stations, ships, and aircraft, which we addressed in Section 3.1.

While the focus of Jin et al. (2024) was on the mid-latitude Southern Hemisphere, we extend our analysis of the mid-latitude diabatic mixing rates to the Northern Hemisphere at the 45×10^{16} kg M_{0e} surface (Fig. 9). ATMs also generally overestimate diabatic mixing rates in the Northern Hemisphere, except during summer (JJA). Whereas MSE-diagnosed mixing rates peak in northern summer, ATM-diagnosed mixing rates have their seasonal minimum at this time. We note that APO gradients in ATMs are close to zero during JJA, leading to poorly defined diabatic mixing rates. We carry out the same transport model and flux product analyses in the Northern Hemisphere in January to March (Fig. 10A) and August to October (Fig. 10B). MIROC4-ACTM still demonstrates the closest agreement with reanalysis data in both seasons, and CTE_TM5 shows the largest mixing rate bias. We note that TM3 and TM5 are based on similar parameterization schemes, but TM3 outperforms TM5. In both seasons, the expected gradients inferred from CESM flux align with the airborne observations, while Jena and DISS overestimate and underestimate expected gradients, respectively.

Our attempt to diagnose mixing rates in ATMs in the Northern Hemisphere mid-latitudes using ocean tracers alone is partly limited by the predominantly land surface. We find both summer and winter peaks in seasonal diabatic mixing rates in the northern mid-latitudes, driven by strong convection. Over land, convection peaks in summer due to strong surface heating that creates unstable atmospheric conditions. Over the ocean, however, convection peaks in winter due to larger air-sea temperature differences. Our ATM-diagnosed mixing rates in the Northern



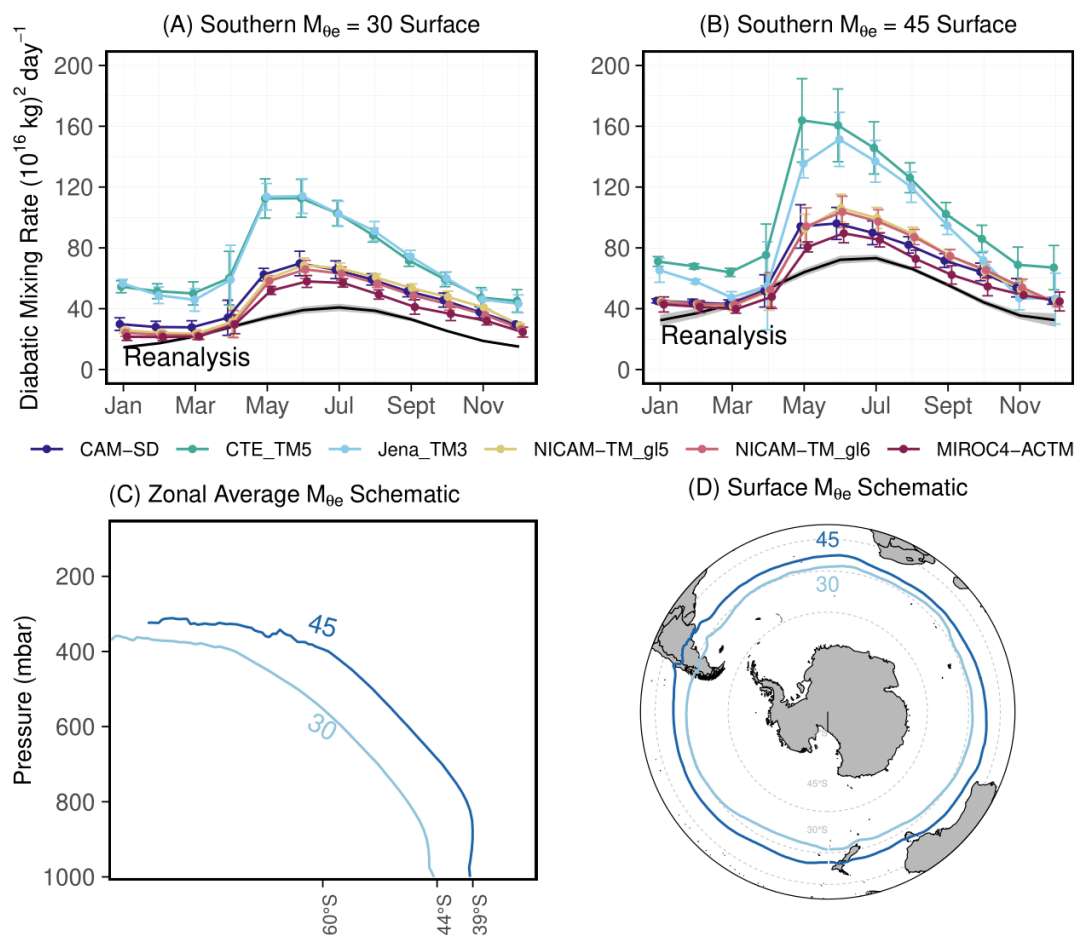
629 Hemisphere may not capture the summer peak because atmospheric mixing processes over land
630 may not be adequately reflected in transport of air-sea APO flux signals, which occurs initially
631 over the ocean. This limitation is particularly significant in the Northern Hemisphere, where
632 zonal mixing is slower (2-4 weeks) due to topographic blocking and stationary wave patterns.
633 We plan to diagnose the land and ocean contrast in atmospheric diabatic mixing in the next
634 APO-MIP1 by also forward transporting land tracers (e.g., CO₂ sources/sinks from the land
635 biosphere). Our method is more robust in the Southern Hemisphere mid-latitudes due to faster
636 zonal mixing (1-2 weeks) and the predominantly ocean surface. We also note that the distinct
637 thermal capacities of land and ocean in the Northern Hemisphere create more complex surface
638 M_{0e} outcrops with larger latitudinal shifts across seasons (Jin et al., 2021), as shown in Fig. 9C.
639 We, however, account for these shifts in our analysis.

640 Our analysis reveals that the ATM-diagnosed diabatic mixing rate primarily reflects an intrinsic
641 characteristic of the transport model, at least in the Southern Hemisphere, showing little
642 sensitivity to the underlying flux pattern, tracers, and land-ocean differences, particularly in
643 models with smaller mixing rates (i.e., two versions of NICAM-TM, MIROC4-ACTM, and
644 CAM-SD). These four models demonstrate consistent mixing rates across different flux products
645 (Figs. 8 and 10). This consistency is further supported by our analysis of diagnosed mixing rates
646 for individual APO components (ΔO_2^{ocn} , ΔN_2^{ocn} , ΔCO_2^{ocn} , ΔO_2^{ff} , and ΔCO_2^{ff}) transported by ATMs
647 with smaller mixing rates, which yields similar mixing rates despite these tracers having distinct
648 signs, seasonal patterns, and magnitudes (Fig. S6). However, ATMs with faster mixing rate (e.g.,
649 Jena_TM3 and CTE_TM5) show large variability both across flux products (Fig. 9-10) and
650 across tracers (Fig. S6). Notably, these two models exhibit approximately 50% slower diagnosed
651 mixing rates for the fossil fuel CO₂ tracer (ΔCO_2^{ff}) compared to the other ocean flux tracers in the
652 austral summer at the 30×10^{16} kg M_{0e} surface. We note that the fossil fuel CO₂ tracer has its
653 main source in the Northern Hemisphere, and its mixing at the mid-latitude Southern
654 Hemisphere preferentially occurs in the upper troposphere. In contrast, the air-sea flux tracers
655 have significant sources/sinks over the Southern Ocean with rapid cross-isentrope mixing
656 preferentially in the lower troposphere. This behavior suggests that these models simulate
657 distinctly different mixing patterns between the planetary boundary layer (0-2 km) and the free
658 troposphere. Specifically, these models appear to have excessive vertical mixing in the boundary



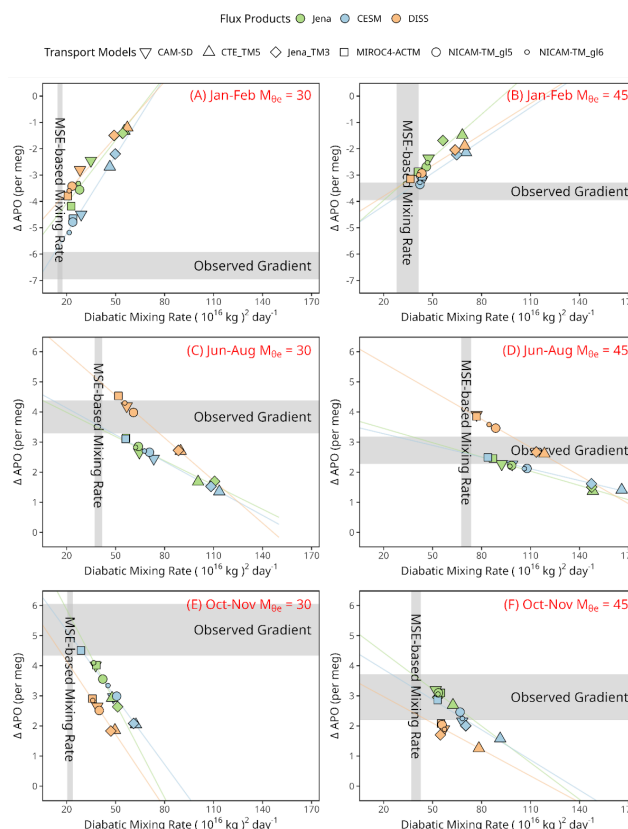
659 layer while maintaining more realistic transport in the free troposphere. Our method, however,
660 assumes a constant cross- M_{θ_e} diabatic mixing rate over the entire M_{θ_e} surface. The excessive
661 boundary layer mixing causes the diagnosed mixing rates in these models to be overly sensitive
662 to the specific vertical distribution of air-sea APO flux components.

663 Our evaluation of ATMs using simulations from APO-MIP1 advances the original framework of
664 Jin et al. (2024) in three key aspects. First, we expand the experimental design by increasing the
665 number of participating ATMs to six and employing three different flux fields with each ATM,
666 generating 18 model realizations. This comprehensive matrix of simulations enables a more
667 systematic evaluation of both transport and flux-related biases. We demonstrate how atmospheric
668 tracer observations can be leveraged to independently evaluate and distinguish between biases in
669 surface fluxes and atmospheric transport models. Second, we enhance the robustness of our
670 MSE-diagnosed mixing rate calculations by incorporating two additional reanalysis products and
671 computing mixing rates at the native high resolution of each reanalysis, rather than averaging to
672 a coarser grid before the calculation. One limitation in our method is that we only use M_{θ_e}
673 calculated from MERRA-2 for each of the transport models rather than using M_{θ_e} calculated
674 from the individual transport model, which in principle can be done by interpolating the
675 temperature and humidity from parent reanalysis to the ATM grid. This limitation would lead to
676 slight inconsistency between the actual M_{θ_e} in the model and the value we assigned to it.
677 However, the differences between M_{θ_e} calculated from different reanalyses remain small and our
678 method ensures consistency in geography of each M_{θ_e} surface (Jin et al., 2021).



679

680 Figure 7: Climatological monthly diabatic mixing rates across the (A) 30 and (B) 45 (10^{16} kg)
 681 M_{θ_e} surfaces in the Southern Hemisphere. ATM-diagnosed mixing rates are derived from six
 682 ATMs in APO-MIP1 that provide 3-D APO fields. Error bars represent the 1σ spread across the
 683 30 and $45 \times 10^{16} \text{ kg } M_{\theta_e}$ of three flux products used here. Black lines represent MSE-diagnosed
 684 mixing rates as the average of four reanalysis MSE budgets, while the gray shaded regions
 685 represent the 1-sigma spread. (C) Schematic showing latitude-pressure distribution of
 686 troposphere zonal annual average M_{θ_e} , and (D) annual average near-surface M_{θ_e} contours of the
 687 30 and 45 (10^{16} kg) surfaces, computed from MERRA-2 reanalysis for the year 2009. These two
 688 M_{θ_e} surfaces have very small seasonal meridional variability.



689

Figure 8: Using MSE-based diabatic mixing rates and airborne observations of cross-isentropic APO gradients to evaluate ATMs and flux models. Each panel compares model-diagnosed diabatic mixing rates (x-axis) and cross- M_{0e} APO gradients (y-axis) at the 30×10^{16} kg M_{0e} surface (A, C, E, $\sim 44^\circ\text{S}$ surface outcrop) and at 45×10^{16} kg M_{0e} (B, D, F, $\sim 39^\circ\text{S}$ surface outcrop). Results are shown for three seasonal periods: Jan-Feb (a-b), Jun-Aug (c-d), and Oct-Nov (e-f) based on available airborne campaigns. Points represent individual model simulations, with colors indicating flux products (Jena, CESM, DISS) and symbols denoting different ATMs. Vertical gray bands show the 1σ range of MSE-based mixing rates derived from four reanalysis products. Horizontal gray bands indicate the 1σ range of observed APO gradients after spatial and temporal bias correction. Colored lines show linear fits of mixing rates and APO gradients for each flux product across different transport models.

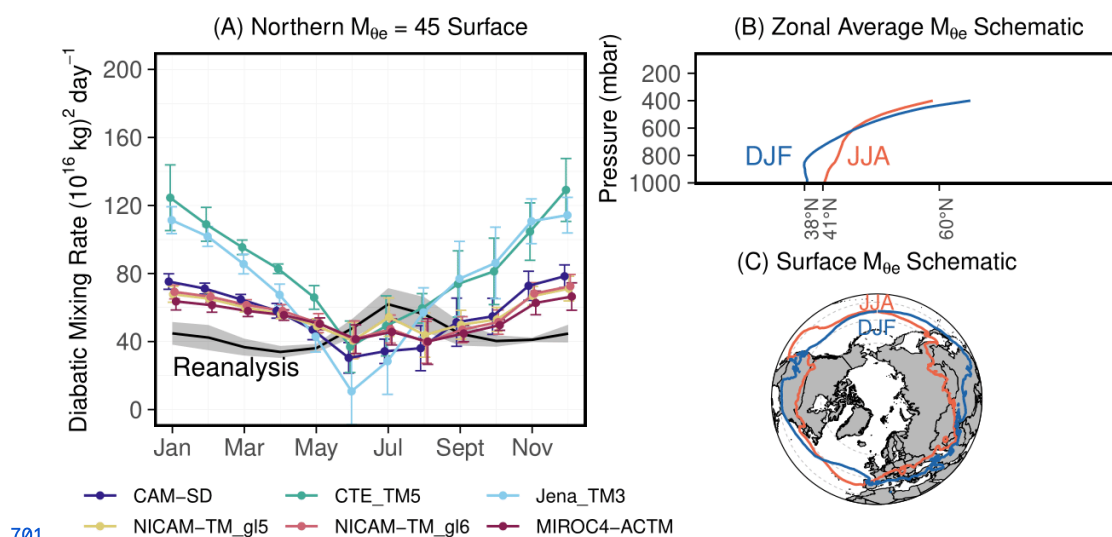
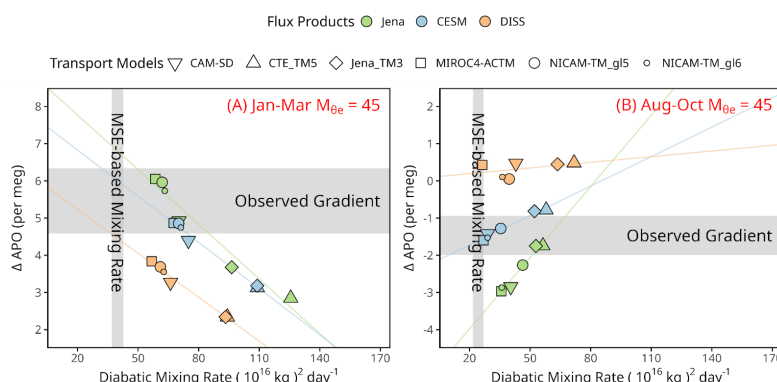


Figure 9: (A) Similar to Fig. 7, but showing climatological monthly diabatic mixing rates across the 45 (10^{16} kg) M_{0e} surface in the Northern Hemisphere. We note that JJA diabatic mixing rates in ATMs are poorly constrained due to close-to-zero cross- M_{0e} APO gradients. (B) Latitude-pressure distribution of zonal average $45 \times 10^{16} \text{ kg}$ M_{0e} surfaces during boreal summer (JJA) and winter (DJF). The two M_{0e} surfaces end at the tropopause, which is higher in the summer in the mid-latitudes. (C) Corresponding Earth surface outcrops of the JJA and DJF $45 \times 10^{16} \text{ kg}$ M_{0e} surfaces. Unlike in the Southern Hemisphere where seasonal meridional variations in M_{0e} surfaces are small, the Northern Hemisphere shows pronounced seasonal shifts due to different land/ocean heating and cooling cycles.



711

712 Figure 10: Similar to Fig. 8, but showing diabatic mixing rates and cross- M_{θ_e} APO gradients in
 713 the Northern Hemisphere late winter / early spring (A) and late-summer / early fall (B) of the 45
 714 $\times 10^{16}$ kg M_{θ_e} surface. We choose January to March and August to October due to sufficient
 715 aircraft sampling and maximum cross- M_{θ_e} APO gradients in these months.

716 3.3. Shipboard model-observation comparison over the Drake Passage

717 The APO-MIP1 simulations could not reproduce latitudinal variations in APO seasonal cycle
 718 amplitude observed from shipboard measurements from 53 to 65°S over the Drake Passage and
 719 adjacent to Tierra del Fuego and the Antarctic Peninsula. Observations reveal a strong
 720 meridional SCA gradient (-2.1 per meg deg^{-1} , with deg positive northward), with SCA increasing
 721 sharply towards higher southern latitudes (Fig. 11). Model simulations substantially
 722 underestimate this latitudinal gradient (Fig. 11), showing weaker slopes averaged across ATMs
 723 of -1.2 (Jena), -0.5 (CESM), and 0.8 (DISS) per meg deg^{-1} . Notably, these gradients remain
 724 generally consistent across different ATMs for each flux product (± 0.26 , ± 0.13 , and ± 0.29 per
 725 meg deg^{-1} , respectively), suggesting this may predominantly be a result of zonal-scale latitudinal
 726 biases in flux seasonality. Underrepresentation of enhanced summertime productivity along the
 727 coast of the Antarctic Peninsula in flux products could also play a role. However, the Gould
 728 typically only transits waters with elevated chlorophyll south of approximately 62°S while the
 729 gradient biases appear further north. Furthermore, seasonally, the SCA biases are caused more by
 730 underestimation of the winter/spring drawdown in APO at high latitudes, rather than the smaller
 731 underestimation of summertime APO enhancement (Figs. S10-11). For CESM, this bias could



originate from incomplete process representation in the ocean biogeochemistry model and the underestimation of winter mixed-layer depths in the Pacific sector of the Southern Ocean, which has historically been a problem for Earth System Models (Sallée et al., 2013). The Jena flux product provides the closest match to the observed SCA gradient. However, several limitations remain, which likely stem from the coarse spatial resolution, limited atmospheric observational constraints over the Southern Ocean, and underrepresentation of mixing patterns around the PSA station (see details below and in SI). The DISS flux product is biased due to its underlying assumptions and sparse observational constraints, as discussed in Jin et al. (2023).

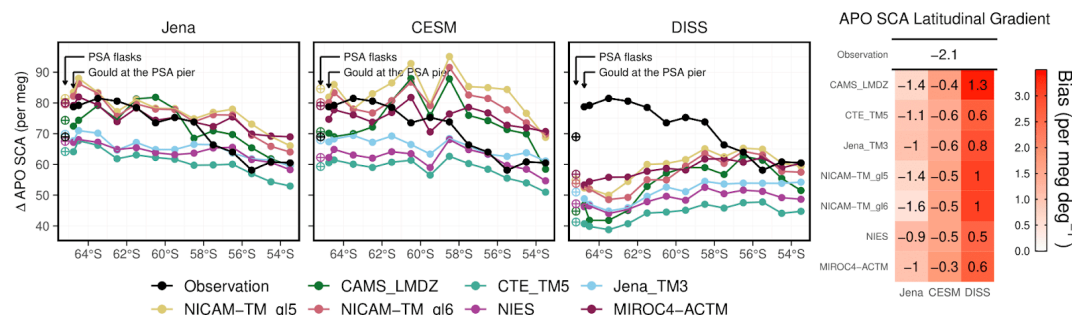
Across ATMs, we find systematic differences of up to $\pm 20\%$ in simulated mean SCA for the entire ship transects over the Drake Passage, independent of the input flux field, with CTE_TM5 consistently producing the smallest SCA and NICAM-TM_gl5 showing the largest. These differences across ATMs are likely caused by differences in marine boundary-layer ventilation in the models. Near-surface mixing over the Southern Ocean is challenging to model, owing to complex boundary-layer structure, strong wind shear, frequent storm systems, SST variations, and poorly represented clouds (Hyder et al., 2018; Knight et al., 2024; Lang et al., 2018; Truong et al., 2020). The coarse-resolution models used here may struggle to capture such phenomena, and the resulting variations in the concentration or dilution of flux signals near the surface drives differences in mean APO SCA. The systematic spread also likely reflects biases in the representation of large-scale diabatic mixing over the high southern latitudes. Models with strong diabatic mixing rates, such as TM5, tend to dilute the meridional gradient of seasonal amplitude through excessive mixing with lower-latitude air masses that have smaller SCAs, resulting in reduced amplitudes at high southern latitudes.

We find that observed SCA at PSA (64.5°S) from SIO flask measurements (~ 70 per meg, averaged from 2012 to 2017) is significantly smaller than nearby ship data from 64°S to 65°S (~ 80 per meg). However, model simulations suggest similar values for both locations. The shipboard measurements are closely tied to the SIO O₂ calibration scale, and any remaining scale differences would be unlikely to affect the seasonal APO SCA. Rather, the observed SCA difference occurs because SIO flask samples collected at PSA predominantly sample descending air masses from the east that have passed over Anvers Island and the Antarctic Peninsula, with peaks above 2000 m (characterized by small APO SCA), whereas the ship samples marine



762 boundary layer air including that over highly productive ocean regions (large APO SCA). As
763 shown in Figs. S7-9, the SIO flasks are collected from the Terra Lab, on the east side of the
764 station, with a wind selection criteria of 5-205°. Even while docked at Palmer (left-most points in
765 Fig. 11), the Gould measurements show elevated SCA compared to PSA flask samples, because
766 the pier is located to the west of the station with samples filtered to exclude air influenced by the
767 station (Figs. S7-9). None of the ATMs, regardless of the flux product used, could reconstruct
768 this feature, even though the models were sampled at the flask collection times. This difference is
769 consistent with that seen between 900-mbar airborne samples and PSA flasks (Fig. 5E). The
770 systematic bias points to the lack of resolution or physics that would be necessary, in either the
771 reanalysis products or the ATMs, to accurately capture fine-scale circulation patterns,
772 particularly the distinct air mass origins affecting ship versus station measurements. We note that
773 the Jena flux product has been optimized to match seasonal APO cycles at Cape Grim
774 Observatory (41°S) and at PSA (64.5°S), which may be the reason for its better performance on
775 the SCA latitudinal gradient. It may do even better if the shipboard data were used in the
776 inversion or if the effective sampling altitude of the SIO flasks at PSA were better accounted for.

777 Our analysis underscores the need for improvements in both ocean biogeochemistry models and
778 ATMs. Future ocean process model developments should include improving accuracy of winter
779 mixed-layer depths and higher-resolution ocean models with enhanced process representation to
780 capture the fine-scale productivity patterns in the Southern Ocean. Additionally, current
781 atmospheric transport models require improved resolution and physics to better represent the
782 complex circulation patterns characteristic of coastal regions.



783

784 Figure 11: Latitudinal distribution of APO SCA across the Drake Passage region (53°S-65°S)
 785 derived from ship observations and model simulations. We calculate SCA by grouping
 786 observations and model simulations into 1 deg latitude bands, shown as points. Model results are
 787 color-coded by ATM and organized by flux products in separate panels. The full seasonal cycles
 788 of observed and simulated APO of these latitude bands are shown in Fig. S10. We also show
 789 SCA observed and simulated for the PSA flask record as open crossed circles (~64.5°S, shifted
 790 0.7° south for visibility), and for ship data while the Gould is docked at or close to the PSA pier
 791 (left-most points, calculated by selecting data from 64.82°S to 64.72°S and 64.1°W to 64.0°W).
 792 The right-most three bands (53°S to 55°S) are typically downwind of Tierra del Fuego (Figs.
 793 S7-9). Both observational and model data for each latitude band or at PSA were detrended using
 794 corresponding cubic smooth spline fits from SPO. SCA was calculated using two-harmonic fits.
 795 The rightmost panel shows the SCA latitudinal gradients (per meg deg⁻¹) from 53°S to 65°S, with
 796 red shading indicating model biases relative to observations. The gradient is calculated as linear
 797 fits of SCA from 53°S to 65°S for each ATM and flux product pair, and the observations. We
 798 exclude CAM-SD in this analysis because the ship data simulation is only available from 2012 to
 799 2015 (i.e., missing 2016 to 2017 data).

800 3.4. Implications for APO and CO₂ inversions and ATM development

801 Our study motivates a community effort to conduct APO inversions. Estimates of spatial and
 802 temporal variations in APO fluxes can improve our understanding of ocean biogeochemical
 803 processes and heat transport, and support verification of fossil-fuel emission estimates (Pickers et
 804 al., 2022; Rödenbeck et al., 2023). Currently, only one global-scale APO inversion product from
 805 Jena CarboScope (Rödenbeck et al., 2008) exists. This product shows excessive seasonal flux



806 amplitudes (Fig. 2) in the tropics and northern mid-latitudes (~ 30 to 60°N) relative to the other
807 two flux products, which are more consistent with aircraft observations (Figs. 8 and 9). These
808 biases in Jena APO inversion partly result from limitations in the TM3 model, which exhibits
809 excessive vertical mixing, particularly in the eastern North Pacific, too rapid diabatic mixing in
810 the southern mid-latitudes, and underrepresentation of monsoon dynamics primarily due to
811 coarse resolution (Jin et al., 2023). The large spread and biases in ATMs shown in this study
812 highlight the importance of developing APO inversions using different ATMs and
813 methodologies, as this will improve our ability to fully assess methodological uncertainties and
814 potential biases in inverted air-sea APO flux estimates.

815 We encourage future inversion efforts to also assimilate column-mean data from airborne
816 campaigns, in addition to sparse surface stations, especially for studying climatological seasonal
817 fluxes. Our study finds that forward simulations from ATMs generally show large spread at
818 northeastern Pacific sites, particularly at LJO and CBA (Fig. 2), where simulations are sensitive
819 to model representation of the marine boundary layer and vertical mixing. The Scripps APO
820 observation network consists mainly of stations along a Pacific transect close to the primary
821 oceanic sources and sinks. Given this limited spatial coverage and our findings of significant
822 vertical mixing biases (e.g., at CBA and LJO) and local wind-direction biases (e.g., at LJO and
823 PSA) in ATMs at the station level, APO inversions that rely solely on these surface observations
824 may be subject to large representation errors. Airborne data, however, provide larger surface
825 footprints and column average metrics that are much less sensitive to vertical mixing biases. Our
826 analysis shows that ATMs are generally consistent with each other in simulating large-scale
827 annual and seasonal column-mean features along flight tracks (Fig. 6). Thus, inversions
828 configured to assimilate airborne column-mean observations would be promising. Further
829 improvement could also be achieved by incorporating shipboard observations to expand zonal
830 coverage, such as from the Gould, across the Atlantic (Pickers et al., 2017), and in the Western
831 Pacific (Tohjima et al., 2012). The study of Jin et al. (2023) used a different configuration of the
832 Jena inversion that also assimilated Japanese ship-based observations across the western Pacific
833 (Tohjima et al., 2012) from 40°S to 50°N . Forward transport of APO fluxes in that configuration
834 aligns better with station and airborne data compared to the configuration used in this study,
835 particularly in reducing the SCA bias in the tropics, suggesting better flux representations.



Biases in diabatic mixing diagnosed from ATMs (Section 3.2) imply that CO₂ inversions using these ATMs are also likely biased. A previous study showed that summer-time Southern Ocean CO₂ estimates from inversion products are correlated with corresponding simulated summer-time cross-isentrope CO₂ gradients in inversions (Long et al., 2021). The simulated gradients are shown to be biased too small due to too rapid diabatic mixing bias in ATMs leading to an overestimation of Southern Ocean CO₂ uptake in the summer (Jin et al., 2024). It is likely that biases in ATMs also contribute to the large spread found in OCO-2 MIP and Global Carbon Project (GCP) inversion ensembles (Byrne et al., 2023; Crowell et al., 2019; Friedlingstein et al., 2025; Peiro et al., 2022). We identify several priority areas for understanding biases in ATMs, particularly the inconsistency between diabatic mixing rates diagnosed from the MSE budgets of parent reanalysis and the tracer fields of coarser resolution ATMs identified here. These inconsistencies likely stem from several potential sources: (1) regridding of original reanalyses to the coarser resolution of the ATM grid, (2) for online GCMs using nudging, incomplete matching of the input meteorology, and (3) for offline models, recalculation or parameterization of convective mass fluxes in the coarser ATM. The first potential source of error from regridding could be evaluated by comparing MSE-based diabatic mixing rates from the parent and regridded fields as long as all components of MSE were included in the regridding. The second potential source of error from nudging could be evaluated by comparing MSE-based diabatic mixing rates from the regridded parent model and the nudged online simulation. Finally, the third potential source of error from recalculating or parameterizing vertical mass fluxes could be evaluated by comparing the MSE-based diabatic mixing rates from the regridded parent model and the tracer-based mixing rates from the ATM. It is notable that diabatic mixing rates diagnosed from two online models, MIROC4-ACTM and CAM-SD, which do not require regridding, are generally consistent with observations, with MIROC4-ACTM showing the best performance among all models (Figs. 7-10).

An important consideration is that the real atmosphere mixes MSE and tracers at different spatial and temporal scales. In the Northern Hemisphere, APO fluxes initially mix vertically over oceans, while strong CO₂ fluxes initially mix vertically over land. In contrast, MSE fluxes mix initially over both land and ocean. Due to the large land area in the Northern Hemisphere, the zonal mixing time scale is much longer (~ 2-4 weeks) so that diabatic mixing rates diagnosed from APO or CO₂ tracers could differ from each other and from those diagnosed from MSE



867 tracers. In the Southern Hemisphere mid-latitudes, these potential differences are much smaller
868 due to the predominance of ocean and rapid zonal mixing (~ 1 -2 weeks). In general, the
869 timescales for diabatic mixing are longer than the timescales of zonal mixing, which support our
870 approach of using tracer fluxes over both ocean and land to evaluate zonal-mean diabatic mixing.
871 Future work should also develop metrics for quantifying along-isentrope (adiabatic) transport to
872 complement our understanding of tracer mixing across isentropes. The timescales of adiabatic
873 mixing influences tracer gradients along isentropic surfaces, which in turn affects diabatic
874 mixing differently in the upper versus lower troposphere. It is also necessary to examine the
875 sensitivity of mixing rates to model resolution, particularly vertical levels at the interface
876 between the boundary layer and free troposphere, and boundary layer schemes. These ATM
877 improvements are essential for enhancing both forward simulations and inverse estimates of
878 surface fluxes.

879 **4. Summary and Outlook**

880 We conducted the Atmospheric Potential Oxygen forward Model Intercomparison Project
881 (APO-MIP1) to generate forward simulations of APO and its components using different flux
882 products and eight ATMs. This effort provides model APO simulations at surface stations, along
883 aircraft flight paths, and on ships that can be directly compared with observations. Additionally,
884 we provide 3-D APO fields from six of the eight ATMs. We use simulations from APO-MIP1 to
885 evaluate eight ATMs and three flux products by comparing simulations against observations
886 from surface stations, aircraft, and ships.

887 We find that model simulations of APO seasonal cycles using a given flux product show
888 considerable summer-time spread at northern surface stations, particularly at two eastern Pacific
889 stations, LJO and CBA (Fig. 3). The bias stems from challenges in accurately representing
890 complex atmospheric vertical transport processes, marine boundary layer mixing, and coastal
891 horizontal mixing in these regions. These findings highlight the limitations of current APO
892 inversions that rely on a single ATM (i.e., TM3 used in Jena APO inversion) and sparse surface
893 observations. However, model simulations of column-average APO resolved from sampling
894 aircraft tracks are consistent across different ATMs, emphasizing the importance of airborne
895 measurements for constraining large-scale flux features.



896 Using airborne observations and a moist-isentropic coordinate framework, we demonstrate that
897 most ATMs overestimate diabatic mixing rates in the mid-latitudes of both hemispheres when
898 compared to mixing rates derived from energy budgets of reanalyses. Among all ATMs used
899 here, Jena_TM3 and CTE_TM5 show the largest biases. These constraints also enable us to
900 separate flux biases from transport-related biases, allowing independent evaluation of flux
901 models, which show that the CESM flux product is the best among the three flux products used
902 in this study. This prognostic model outperforms two observation based products because of
903 sparse atmospheric and surface observations, limitations in ATM used in atmospheric inversion,
904 and because seasonal APO fluxes are driven by physical and biological processes that CESM
905 represents well.

906 We encourage the broader community to develop new APO inversions, which could provide
907 independent constraints on ocean biogeochemical processes and improve our understanding of
908 the ocean carbon sink. Model simulations from APO-MIP1 can be used in other applications,
909 including the calibration of methods for estimating seasonal air-sea APO fluxes from global
910 atmospheric observations (e.g., Jin et al., 2023), constraining the representation of regional to
911 global marine production in Earth system models (e.g., Nevison et al., 2012, 2015, 2018), and for
912 understanding ESM biases in seasonal air-sea CO₂ exchange related to both thermal and
913 non-thermal forcings. The transport simulations can also support the evaluation of long-term
914 trends in O₂:CO₂ ratios over the Southern Ocean based on surface station gradients, useful for
915 assessing biogeochemical responses to climate change.

916 We expect APO-MIP1 to continue evolving as an active collaboration examining atmospheric
917 tracer transport and air-sea O₂ flux estimates. The current implementation excluded the air-sea
918 CO₂ component and long-term flux trends from the Jena flux product, and does not include
919 interannual and long-term flux trends in the DISS flux product, making these simulations
920 unsuitable for interpreting interannual to long-term air-sea O₂ fluxes features. Thus, we only
921 analyze APO seasonal cycles and meridional gradients here. The next phase of APO-MIP1 will
922 address these limitations by incorporating updated inversion flux fields based on a larger set of
923 atmospheric APO observations and including interannual variability. We will expand the scope
924 by including terrestrial O₂ flux fields for O₂-specific analyses and seasonal-only component
925 fluxes to investigate rectifier effects. Additionally, we plan to update air-sea O₂ fluxes derived



from surface ocean dissolved oxygen measurements by replacing Garcia and Keeling (2001) with fluxes calculated from recent machine learning interpolation of dissolved oxygen products (Gouretski et al., 2024; Ito et al., 2024; Sharp et al., 2023). We encourage broader participation from diverse modeling groups in the next phase of APO-MIP1.

Appendix A: Surface station, airborne, and shipboard APO measurements.

The surface station APO observations from the Scripps O₂ program have been described in Keeling et al. (1998). Briefly, flask triplicates have been collected at biweekly to monthly frequency during clean background air conditions at a network of sites for over three decades, and returned to Scripps for analysis using interferometric and mass-spectrometric techniques. Here we use monthly data that was averaged from roughly bi-weekly data. The flask measurements are first adjusted to the middle of each month, parallel to the mean seasonal cycle for that station, before averaging. The APO-MIP1 output for these stations was reported matching the ObsPack CO₂ files from the Scripps O₂ Program, to take advantage of the established ObsPack format. These CO₂ measurements correspond to the same flask air on which O₂ is measured. The model output is treated in the same way as the observations to generate monthly means.

Airborne APO measurements from HIPPO, ORCAS, and ATom campaigns were made in situ with the NSF NCAR Airborne Oxygen Instrument (AO2), using a vacuum-ultraviolet absorption technique to measure O₂ and a single-cell infrared gas analyzer to measure CO₂ (Stephens et al., 2021). AO2 produces measurements every 2.5 s, which are averaged to 10 sec frequency for merging with other aircraft data. To correct for flight-specific sampling offsets, the in situ AO2 data were adjusted to agree with flask measurements collected during each flight using the NSF NCAR / Scripps Medusa flask sampler on a flight-by-flight average basis (Jin et al., 2023; Stephens et al., 2021).

HIPPO and ATom had nearly pole-to-pole coverage, and from near surface (150 - 300 m) to above the tropopause. HIPPO consisted of five campaigns between 2009 and 2011, and most data were collected above the Pacific. ATom consisted of four campaigns between 2016 and 2018, and each campaign had a Pacific transect and an Atlantic transect. ORCAS was a 6-week campaign with dense temporal sampling over the Drake Passage and ocean areas adjacent to the



tip of South America and the Antarctic Peninsula. The APO-MIP1 output for these aircraft measurements was reported matching the ObsPack CO₂ files for each campaign. These data are also at 10 sec frequency but correspond to different instruments with different calibration intervals. To match the observed and model time series, we mask observations when model output is not available, and vice versa. We also exclude any stratospheric data, with the stratosphere defined as water vapor concentrations below 50 ppm and either ozone concentrations exceeding 150 ppb, or detrended N₂O levels (normalized to 2009) below 319 ppb (Jin et al., 2021). Water vapor and ozone were measured by the NOAA UAS Chromatograph for Atmospheric Trace Species instrument (Hintsa et al., 2021). N₂O was measured by the Harvard Quantum Cascade Laser System instrument (Santoni et al., 2014). We filter the airborne data to exclude continental or urban boundary-layer air sampled while landing, taking off, or conducting missed approaches at airports (Jin et al., 2021).

Shipboard APO measurements from the ARSV *L. M. Gould* were made in situ during over 90 transects of Drake Passage on 50 cruises between 2012 and 2017 using a fuel-cell method for O₂ and a two-cell non-dispersive infrared gas analyzer for CO₂. The instrumentation was similar to a previously developed tower system (Stephens et al., 2003), but adapted and optimized for shipboard use. The instrument produces measurements at 1 min frequency. The cruises occurred in all months of the year but are more sparse during austral winter. The Gould operated almost exclusively between Punta Arenas, Chile and Palmer Station, Antarctica, in support of resupplying and transferring personnel to Palmer Station. The cruises span from 53° to 65°S in all months, and extend as far as 70°S during summer months. The APO-MIP1 output for the Gould was reported matching the ObsPack CO₂ file from the NOAA underway pCO₂ system. This system measures atmospheric CO₂ for 15 min every two hours. To match the observed and model time series, we first calculate hourly means for each and then mask observations when model output is not available, and vice versa.



980 Appendix B: APO flux products

981 B.1. Air-sea APO flux products

982 The first air-sea APO flux product (Jena) is air-sea APO flux from the Jena CarboScope APO
983 Inversion (version ID: apo99X_v2021), which is available directly as F_{APO}^{ocn} (update of
984 Rödenbeck et al., 2008). In this inversion, the posterior fluxes (variable name: apoflux_ocean)
985 were optimized to best match observed APO at 9 stations in the Scripps O₂ Program surface
986 network (Manning & Keeling, 2006) and at 2 stations from the National Institute for
987 Environmental Studies (Tohjima et al., 2012). The prior air-sea CO₂ flux was not included in the
988 forward simulations here. We note that the exclusion of prior air-sea CO₂ flux has only minimal
989 impact on the simulated APO seasonal cycle and north-to-south annual gradient but reduces the
990 tropical “bulge” of annual mean by approximately 1 per meg and results in close to zero
991 long-term APO trend. The Jena product is available from 1999 to 2020 originally with spatial
992 resolution of 2° latitude × 2.5° longitude at daily intervals, converted to 1° × 1°. The Jena
993 inversion used the TM3 transport model, which is also one of the models participating in
994 APO-MIP1. In the case of TM3 forward transport simulation, the Jena inversion posterior fluxes
995 have been re-run forward through the ATM, and thus this combination of fluxes and transport
996 should agree well at the surface stations used for inversion optimization.

997 The second air-sea APO flux product (CESM) uses air-sea O₂, CO₂, and N₂ flux components
998 from the Community Earth System Model (CESM2) Forced Ocean-Sea-Ice (FOSI) simulation
999 (Yeager et al., 2022), which is forced by atmospheric fields from JRA55-do reanalysis (Tsuji
1000 et al., 2018) and prognostic ocean biogeochemistry using the Marine Biogeochemistry Library
1001 (MARBL, Long et al., 2021). The model directly produces $F_{O_2}^{ocn}$ and $F_{CO_2}^{ocn}$, while $F_{N_2}^{ocn}$ is
1002 calculated by scaling the ocean heat flux (Q, W m⁻²) output using the relationship from Keeling
1003 and Shertz (1992) following

$$1004 \quad F_{N_2}^{ocn} = - \frac{1}{1.3} \cdot \frac{dS}{dT} \cdot \frac{Q}{C_p}, \quad (B1)$$

1005 where dS/dT (mol kg⁻¹ C⁻¹) is the temperature derivative of solubility using solubility
1006 coefficients from Hamme & Emerson (2004). C_p represents the specific heat capacity of



seawater, which is assumed to be $3993 \text{ J kg}^{-1} \text{ C}^{-1}$. The factor of 1/1.3 is to adjust the seasonal amplitude due to the temporal lag between tracer flux and heat flux, as proposed by Jin et al. (2007).

These three CESM flux components have a resolution of 1° latitude \times 1° longitude grid with the North Pole displaced to Greenland. All fields are available from 1958 to 2020, but we only use fluxes from 1986 to 2020. $F_{O_2}^{ocn}$ and $F_{CO_2}^{ocn}$ are output from the model at daily resolution, whereas $F_{N_2}^{ocn}$ is calculated from monthly model heat fluxes then interpolated to daily resolution. This version of CESM was designed to initialize a seasonal-to-multiyear large ensemble (SMYLE) of coupled simulations for evaluating predictability. It is forced by observed meteorology starting in 1958, at which point it branches off of a FOSI configuration using JRA55-do atmospheric fields as surface boundary conditions (Yeager et al., 2022). The FOSI simulation consists of six consecutive cycles of 1958-2018 forcing, with the sixth cycle (used for SMYLE) extended through 2020. Annual mean heat fluxes from this configuration show a small cooling drift over the historical period, and thus the inferred annual mean and long-term trend of O_2 and N_2 flux should not be interpreted as realistic.

The third air-sea APO flux product (DISS) uses bottom-up air-sea O_2 and CO_2 flux estimates derived primarily from dissolved gas measurements. $F_{O_2}^{ocn}$ consists of a seasonal component calculated from the dissolved O_2 measurement based climatology of Garcia & Keeling (2001), with seasonal amplitude scaled by 0.82 according to Naegler et al. (2006), and an annual mean component from the ocean inversion of Resplandy et al. (2016) for 21 regions using transport from MITgcm-ECCO. The seasonal component ($1.125^\circ \times 1.125^\circ \times$ monthly) was linearly regridded to $1^\circ \times 1^\circ \times$ daily resolution. For the annual mean component, the original regional values (21 regions) were spatially interpolated to $1^\circ \times 1^\circ$ resolution while conserving the total sum within each region, then temporally interpolated to daily values. We use $F_{CO_2}^{ocn}$ from the machine learning interpolation of pCO_2 based air-sea CO_2 fluxes (Jersild et al., 2017; Landschützer et al., 2016). The version of this product that we used provides fluxes from 1982 to 2020, with resolution of 1° latitude \times 1° longitude \times monthly, which we interpolated to daily. We



1034 use Eq. B1 to calculate $F_{N_2}^{ocn}$ with heat fluxes from ERA5 reanalyses (Hersbach et al., 2020),
1035 which is available from 1979 onwards, with resolution of 0.25° latitude \times 0.25° longitude \times
1036 monthly. Sea-surface temperature (SST) estimates required to calculate dS/dT (Eq. B1) are from
1037 World Ocean Atlas (WOA) v2018 with resolution of 1° latitude \times 1° longitude \times monthly. SST is
1038 available as a 1981 to 2010 climatology but we use it repeatedly for 1986 to 2020.

1039 B.2. Fossil fuel APO uptake products

1040 We used two products for F_{APO}^{ff} . The first product (GridFED) uses fossil CO_2 emission and O_2
1041 uptake fluxes from Jones et al. (2021), downloaded from Jones et al. (2022). This product is
1042 available from 1959 to 2020, with resolution of 0.1° latitude \times 0.1° longitude \times monthly, which
1043 we interpolate to daily.

1044 The second product (OCO2MIP) use $F_{CO_2}^{ff}$ as prepared for the OCO-2 Model Intercomparison
1045 Project (MIP) version 10, downloaded from Basu & Nassar (2021), with resolution of 1° latitude
1046 \times 1° longitude \times hourly. This $F_{CO_2}^{ff}$ product uses fossil fuel CO_2 emission from ODIAC (Oda et
1047 al., 2018) for 2000 to 2019. For 2020, the flux was scaled from 2019 using the ratio of 2020 to
1048 2019 global emissions reported by Liu et al. (2020). $F_{O_2}^{ff}$ is not available from this product, but
1049 we scale the atmospheric field of ΔCO_2^{ff} by a factor of -1.4 to estimate ΔO_2^{ff} (Keeling, 1988;
1050 Steinbach et al., 2011). We primarily use GridFED, except for CAMS_LMDZ where we use
1051 OCO2MIP instead, because $F_{O_2}^{ff}$ from GridFED is missing for years after 2015. The differences
1052 between these two products are negligible compared to the magnitude of ocean-driven APO
1053 variations, for the seasonal metrics considered here.

1054 Appendix C: Calculation of M_{θ_e} , cross- M_{θ_e} diabatic mixing rates and APO 1055 gradients

1056 The mass-indexed moist isentropic coordinate M_{θ_e} is defined as the total dry air mass under a
1057 specific moist isentropic surface (θ_e) in the troposphere of a given hemisphere. Surfaces of



constant M_{θ_e} are parallel to surfaces of constant θ_e but the relationship changes with season, as the atmosphere warms and cools. M_{θ_e} surfaces have air mass (10^{16} kg) as the unit, and are adjusted to conserve dry air mass below the surface at any instant in time. M_{θ_e} is calculated as a function of θ_e and time following

$$M_{\theta_e}(x, t) = \sum M_x(t) | \theta_{e_x} < \theta_e, \quad (C1)$$

where x indicates an individual grid cell of the atmospheric field, $M_x(t)$ is the dry air mass of each grid cell x at time t , and θ_{e_x} is the equivalent potential temperature of the grid cell. For a given θ_e threshold, the corresponding M_{θ_e} value is calculated by integrating the air mass of all grid cells with θ_e value smaller than the threshold. We only integrate air mass in the troposphere, which is defined here as potential vorticity unit (PVU) smaller than 2. At each time step, this calculation yields a unique value of M_{θ_e} for each value of θ_e as well as a 3-D field of atmospheric M_{θ_e} . Following the spatial pattern of θ_e , M_{θ_e} values generally increase from low to high altitudes and from poles to equator. We generate daily M_{θ_e} fields using four different reanalysis products (MERRA-2, JRA-55, JRA-3Q, and ERA5) at their native resolution, avoiding potential information loss from grid interpolation (Gelaro et al., 2017; Hersbach et al., 2020; Kobayashi et al., 2015; Kosaka et al., 2024).

The calculation of diabatic mixing rates in ATMs is based on a box model approach, which uses M_{θ_e} as boundaries. A schematic of the box model is available as Fig. 1 of Jin et al. (2024). The box model invokes tracer air mass balance, which recognizes tracer inventory change (M_i , Tmol) of each M_{θ_e} box equal to the sum of surface fluxes (F_i , Tmol day⁻¹) and the diabatic transport between boxes ($T_{i,i+1}$, Tmol day⁻¹, positive poleward). The transport term is considered as a diffusive system, which is parameterized as the product of diabatic mixing rate across the M_{θ_e} boundary ($D_{i,i+1}$, (10¹⁶ kg)² day⁻¹) and the tracer concentration (χ_{i+1} , Tmol tracer per kg air mass) gradient between two boxes. The full mass balance follows

$$\frac{\partial M_i}{\partial t} = \begin{cases} F_i + T_{i,i+1} & \text{if } i = 1 \\ F_i + T_{i,i+1} - T_{i-1,i} & \text{if } i > 1, \end{cases} \quad (C2)$$

with



$$T_{i,i+1} = D_{i,i+1} \cdot \frac{\chi_{i+1} - \chi_i}{\Delta M_{\theta_e}}. \quad (C3)$$

In these equations, i is the number label of the box and is set to be 1 at the highest latitude, ΔM_{θ_e} is the distance in M_{θ_e} coordinates between box centers, which for evenly spaced boxes as used here, is the same as the total air mass of each box. In this study, we set the range of each M_{θ_e} box to be 15×10^{16} kg air mass, and therefore ΔM_{θ_e} equals the same value. The diabatic mixing rate (D) can be expressed as

$$D_{i,i+1}(t) = \frac{\left[\sum_{i'=1}^{i'=i} \left(\frac{dM_{i'}(t)}{dt} - F_{i'}(t) \right) \right]}{[\chi_{i+1}(t) - \chi_i(t)]} \cdot \Delta M_{\theta_e}. \quad (C4)$$

This method effectively reconstructs large-scale tracer transport features (T) in ATMs, as demonstrated in Jin et al. (2024). We note that the diabatic mixing rate is a property of the corresponding M_{θ_e} and is theoretically insensitive to the choice of box sizes. We calculate climatological monthly average (2009 to 2018) diabatic mixing rates for each of the six transport models using the 3-D APO fields from transporting each of the three flux products (Figs. 7 and 9). To assign M_{θ_e} at the model grid locations and times for each ATM, we always use M_{θ_e} from MERRA-2 interpolated to the ATM grid, to ensure spatial consistency. Using other reanalyses only leads to small ($< 5\%$) differences in ATM-diagnosed diabatic mixing rates (Jin et al., 2024).

Independent observational constraints on ATM-diagnosed mixing rates are calculated from moist static energy (MSE) budgets of four meteorological reanalyses (Figs. 7 and 9). MSE is a measure of static energy that is conserved in adiabatic ascent/descent and during latent heat release due to condensation, and naturally aligns with surfaces of θ_e or M_{θ_e} . This diagnostic approach offers more robust mixing rate estimates than tracer-based methods in part because MSE maintains consistent, non-zero gradients at each reanalysis time step, unlike chemical tracers. Additionally, MSE-based mixing rates are directly diagnosed from reanalysis on the original grid, avoiding potential artifacts introduced when these fields are interpolated to coarser transport model grids, and any recalculation of vertical mass fluxes and subgrid-scale mixing parameterizations in ATMs.



The MSE-diagnosed mixing rate calculation adapts our tracer box model framework. In this adaptation, we replace tracer inventory (M_i , Tmol) by MSE (S_i , J), replace surface tracer flux (F_i , Tmol day⁻¹) by surface heat flux (Q_i , J day⁻¹), and add an additional term to account for atmospheric radiative energy balance (R_i , J day⁻¹), following

$$D_{i,i+1}(t) = \frac{\left[\sum_{i'=1}^{i'=i} \left(\frac{dS_{i'}(t)}{dt} - Q_{i'}(t) - R_{i'}(t) \right) \right]}{[\chi_{i+1}(t) - \chi_i(t)]} \cdot \Delta M_{\theta_e} \quad (C5)$$

We note that the gradient on the denominator in Eq. C5 represents the MSE density gradient (J per kg air mass) across the M_{θ_e} surface. The calculation of these terms requires air temperature, specific humidity, surface heat flux, including surface sensible and latent heat flux, and radiative imbalance from reanalysis. Further details on the process to diagnose mixing rate from both ATMs and reanalyses can be found in Jin et al. (2024).

The cross- M_{θ_e} APO gradient was calculated using data grouped into two adjacent boxes in the M_{θ_e} space, with box centers spanning 15×10^{16} kg air mass across the target surface boundary. For each box, we calculate the average APO concentration by trapezoidal integration of detrended APO as a function of M_{θ_e} and dividing by the M_{θ_e} range (Jin et al., 2021). We carry out the calculation for each airborne campaign, using the observations, model flight track output, and 3-D model fields. Flight-track estimated cross- M_{θ_e} APO gradients are not directly comparable to simulated gradients from full 3-D fields, due to spatial and temporal coverage biases in airborne observations. We correct for both biases in the APO airborne observations and model flight track output (detailed in Supplement Text S1).

Code and Data Availability

The 10 components of air-sea APO flux and fossil fuel APO uptake products, and the output of ATM forward transport simulations of these 10 components, including ATM samples at surface stations, ship transects, aircraft measurements, and 3-D atmospheric fields, are available at <https://doi.org/10.5065/f3pw-a676> (Stephens et al., 2025). APO observations at surface stations from the Scripps O₂ network are available at <https://doi.org/10.6075/J0WS8RJR> (Keeling, 2019). All HIPPO 10-s merge data are available from Wofsy, 2017. Here we use updated HIPPO AO2



1138 data from (Stephens et al., 2021a, 2021b, 2021c, 2021d, 2021e). All ORCAS 10-s merge data are
1139 available at Stephens (2017). Here we use updated ORCAS AO₂ data from Stephens et al.
1140 (2021f). All ATom 10-s merge data are available at <https://doi.org/10.3334/ORNLDAAC/1925>
1141 (Wofsy, 2021), including the version of AO₂ data used here. O₂ and CO₂ measurements from
1142 ARSV Gould are available at <https://doi.org/10.26023/FDDD-PC3X-4M0X> (Stephens, 2025).
1143 Note that airborne O₂/N₂ data are all on the Scripps O₂ Program SIO2017 O₂/N₂ scale defined on
1144 March 16, 2020, surface station data are on the SIO2023 O₂/N₂ scale defined on August 30, 2024,
1145 and shipboard data are on the SIO2023 O₂/N₂ scale defined on August 30, 2024. Airborne CO₂
1146 measurements are on the WMO X2007 CO₂ scale, while station and shipboard CO₂ data are on
1147 the WMO X2019 CO₂ scale. The use of different scales has only minor impacts on interpreting
1148 APO seasonal cycles and latitudinal gradients. Code used to produce input flux files and to
1149 post-process submitted ObsPack files is available at <https://doi.org/10.5065/f3pw-a676> (Stephens
1150 et al., 2025).

1151 Acknowledgments

1152 We would like to acknowledge the efforts of the full HIPPO, ORCAS, and ATom science teams
1153 and the pilots and crew of the NSF NCAR GV and NASA DC-8, as well as the NSF NCAR and
1154 NASA project managers, field support staff, and logistics experts. Atmospheric O₂ measurements
1155 on HIPPO were supported by NSF grants ATM-0628519 and ATM-0628388. ORCAS was
1156 supported by NSF grants PLR-1501993, PLR-1502301, PLR-1501997, and PLR-1501292.
1157 Atmospheric O₂ measurements on ATom 1 were supported by NSF grants AGS-1547626 and
1158 AGS-1547797. Atmospheric O₂ measurements on ATom 2-4 were supported by NSF
1159 AGS-1623745 and AGS-1623748. The recent atmospheric measurements of the Scripps O₂
1160 program have been supported via funding from the NSF and the National Oceanographic and
1161 Atmospheric Administration (NOAA) under Grants OPP-1922922 and NA20OAR4320278,
1162 respectively. The atmospheric O₂ measurements from ARSV Laurence M. Gould were supported
1163 by NSF grants ANT-0944761, PLR-1341425, and PLR-1543511. For sharing O₃, N₂O, and H₂O
1164 measurements, we thank Jim Elkins, Eric Hintsa, and Fred Moore for ATom-1 N₂O data;
1165 Ru-Shan Gao and Ryan Spackman for HIPPO O₃ data; Ilann Bourgeois, Jeff Peischl, Tom
1166 Ryerson, and Chelsea Thompson for ATom O₃ data; Stuart Beaton, Minghui Diao, and Mark
1167 Zondlo for HIPPO and ORCAS H₂O data; and Glenn Diskin and Joshua DiGangi for ATom H₂O



data. YJ would like to acknowledge the Advanced Study Program Postdoctoral Fellowship in the NSF National Center for Atmospheric Research. This material is based upon work supported by the NSF National Center for Atmospheric Research, which is a major facility sponsored by the U.S. National Science Foundation under Cooperative Agreement No. 1852977. The work of FC was granted access to the HPC resources of CCRT under the allocation CEA/DRF, and of TGCC under the allocation A0130102201 made by GENCI. NC and PKP are supported by the Environment Research and Technology Development Fund (grant no. JPMEERF24S12205) and Arctic Challenge for Sustainability II (ArCS-II) project (grant no. JPMXD1420318865). YN is supported by JSPS KAKENHI (grant no. JP22H05006, JP80282151) and the Environment Research and Technology Development Fund (grant no. JPMEERF24S12210). IL and JH were supported by the Netherlands Organisation for Scientific Research (grant no. VI.Vidi.213.143 and NWO-2023.003).

Author Contributions

YJ and BS carried out the research and wrote the paper with input from all co-authors. YJ, BS, and MC designed the research. MC prepared input fluxes for the transport models. BS provided airborne and shipboard observation data. EM provided surface station and airborne observation data. YJ, FC, NC, JH, IL, SM, YN, PP, CR, and JV provided forward transport model simulations. All authors contributed to reviewing and editing the text.

Competing Interests

The contact author has declared that none of the authors has any competing interests.

Reference

Adcock, K. E., Pickers, P. A., Manning, A. C., Forster, G. L., Fleming, L. S., Barningham, T., et al. (2023). 12 years of continuous atmospheric O₂, CO₂ and APO data from Weybourne Atmospheric Observatory in the United Kingdom. *Earth System Science Data*, 15(11), 5183–5206. <https://doi.org/10.5194/essd-15-5183-2023>



- 1193 Bailey, A., Singh, H. K. A., & Nusbaumer, J. (2019). Evaluating a Moist Isentropic Framework
1194 for Poleward Moisture Transport: Implications for Water Isotopes Over Antarctica.
1195 *Geophysical Research Letters*, 46(13), 7819–7827.
1196 <https://doi.org/10.1029/2019GL082965>
- 1197 Baker, D. F., Law, R. M., Gurney, K. R., Rayner, P., Peylin, P., Denning, A. S., et al. (2006).
1198 TransCom 3 inversion intercomparison: Impact of transport model errors on the
1199 interannual variability of regional CO₂ fluxes, 1988–2003. *Global Biogeochemical*
1200 *Cycles*, 20(1). <https://doi.org/10.1029/2004GB002439>
- 1201 Basu, S., & Nassar, R. (2021). Fossil Fuel CO₂ Emissions for the OCO2 Model Intercomparison
1202 Project (MIP) (Version 2020.1) [Data set]. Zenodo.
1203 <https://doi.org/10.5281/zenodo.4776925>
- 1204 Battle, M., Fletcher, S. M., Bender, M. L., Keeling, R. F., Manning, A. C., Gruber, N., et al.
1205 (2006). Atmospheric potential oxygen: New observations and their implications for some
1206 atmospheric and oceanic models. *Global Biogeochemical Cycles*, 20(1), 2005GB002534.
1207 <https://doi.org/10.1029/2005GB002534>
- 1208 Belikov, D. A., Maksyutov, S., Krol, M., Fraser, A., Rigby, M., Bian, H., et al. (2013). Off-line
1209 algorithm for calculation of vertical tracer transport in the troposphere due to deep
1210 convection. *Atmospheric Chemistry and Physics*, 13(3), 1093–1114.
1211 <https://doi.org/10.5194/acp-13-1093-2013>
- 1212 Belikov, D. A., Maksyutov, S., Yaremchuk, A., Ganshin, A., Kaminski, T., Blessing, S., et al.
1213 (2016). Adjoint of the global Eulerian–Lagrangian coupled atmospheric transport model
1214 (A-GELCA v1.0): development and validation. *Geoscientific Model Development*, 9(2),
1215 749–764. <https://doi.org/10.5194/gmd-9-749-2016>



- 1216 Bent, J. (2014). *Airborne Oxygen Measurements over the Southern Ocean as an Integrated*
1217 *Constraint of Seasonal Biogeochemical Processes*. University of California, San Diego.
- 1218 Blaine, T. (2005). *Continuous Measurements of Atmospheric Ar/N₂ as a Tracer of Air-Sea Heat*
1219 *Flux: Models, Methods, and Data*. University of California, San Diego.
- 1220 Byrne, B., Baker, D. F., Basu, S., Bertolacci, M., Bowman, K. W., Carroll, D., et al. (2023).
1221 National CO₂ budgets (2015–2020) inferred from atmospheric CO₂ observations in
1222 support of the global stocktake. *Earth System Science Data*, 15(2), 963–1004.
1223 <https://doi.org/10.5194/essd-15-963-2023>
- 1224 Carroll, D., Menemenlis, D., Adkins, J. F., Bowman, K. W., Brix, H., Dutkiewicz, S., et al.
1225 (2020). The ECCO-Darwin Data-Assimilative Global Ocean Biogeochemistry Model:
1226 Estimates of Seasonal to Multidecadal Surface Ocean *p*CO₂ and Air-Sea CO₂ Flux.
1227 *Journal of Advances in Modeling Earth Systems*, 12(10), e2019MS001888.
1228 <https://doi.org/10.1029/2019MS001888>
- 1229 Chandra, N., Patra, P. K., Niwa, Y., Ito, A., Iida, Y., Goto, D., et al. (2022). Estimated regional
1230 CO₂ flux and uncertainty based on an ensemble of atmospheric CO₂ inversions.
1231 *Atmospheric Chemistry and Physics*, 22(14), 9215–9243.
1232 <https://doi.org/10.5194/acp-22-9215-2022>
- 1233 Chevallier, F. (2013). On the parallelization of atmospheric inversions of CO₂ surface fluxes
1234 within a variational framework. *Geoscientific Model Development*, 6(3), 783–790.
1235 <https://doi.org/10.5194/gmd-6-783-2013>
- 1236 Chevallier, F., Fisher, M., Peylin, P., Serrar, S., Bousquet, P., Bréon, F. -M., et al. (2005).
1237 Inferring CO₂ sources and sinks from satellite observations: Method and application to
1238 TOVS data. *Journal of Geophysical Research: Atmospheres*, 110(D24), 2005JD006390.



- 1239 <https://doi.org/10.1029/2005JD006390>
- 1240 Chevallier, F., Ciais, P., Conway, T. J., Aalto, T., Anderson, B. E., Bousquet, P., et al. (2010). CO₂
- 1241 surface fluxes at grid point scale estimated from a global 21 year reanalysis of
- 1242 atmospheric measurements. *Journal of Geophysical Research*, 115(D21), D21307.
- 1243 <https://doi.org/10.1029/2010JD013887>
- 1244 Chikira, M., & Sugiyama, M. (2010). A Cumulus Parameterization with State-Dependent
- 1245 Entrainment Rate. Part I: Description and Sensitivity to Temperature and Humidity
- 1246 Profiles. *Journal of the Atmospheric Sciences*. <https://doi.org/10.1175/2010JAS3316.1>
- 1247 Crowell, S., Baker, D., Schuh, A., Basu, S., Jacobson, A. R., Chevallier, F., et al. (2019). The
- 1248 2015–2016 carbon cycle as seen from OCO-2 and the global in situ network.
- 1249 *Atmospheric Chemistry and Physics*, 19(15), 9797–9831.
- 1250 <https://doi.org/10.5194/acp-19-9797-2019>
- 1251 Danabasoglu, G., Lamarque, J.-F., Bacmeister, J., Bailey, D. A., DuVivier, A. K., Edwards, J., et
- 1252 al. (2020). The Community Earth System Model Version 2 (CESM2). *Journal of*
- 1253 *Advances in Modeling Earth Systems*, 12(2), e2019MS001916.
- 1254 <https://doi.org/10.1029/2019MS001916>
- 1255 Denning, A. S., Holzer, M., Gurney, K. R., Heimann, M., Law, R. M., Rayner, P. J., et al. (1999).
- 1256 Three-dimensional transport and concentration of SF₆ A model intercomparison study
- 1257 (TransCom 2). *Tellus B: Chemical and Physical Meteorology*, 51(2), 266–297.
- 1258 <https://doi.org/10.3402/tellusb.v51i2.16286>
- 1259 Emanuel, K. A. (1991). A Scheme for Representing Cumulus Convection in Large-Scale
- 1260 Models. *Journal of the Atmospheric Sciences*, 48(21), 2313–2329.
- 1261 [https://doi.org/10.1175/1520-0469\(1991\)048<2313:ASFRCC>2.0.CO;2](https://doi.org/10.1175/1520-0469(1991)048<2313:ASFRCC>2.0.CO;2)



- 1262 Faassen, K. A. P., Nguyen, L. N. T., Broekema, E. R., Kers, B. A. M., Mammarella, I., Vesala, T.,
1263 et al. (2023). Diurnal variability of atmospheric O₂, CO₂, and their exchange ratio above a
1264 boreal forest in southern Finland. *Atmospheric Chemistry and Physics*, 23(2), 851–876.
1265 <https://doi.org/10.5194/acp-23-851-2023>
- 1266 Faassen, K. A. P., Vilà-Guerau de Arellano, J., González-Armas, R., Heusinkveld, B. G.,
1267 Mammarella, I., Peters, W., & Luijkx, I. T. (2024). Separating above-canopy CO₂ and O₂
1268 measurements into their atmospheric and biospheric signatures. *Biogeosciences*, 21(12),
1269 3015–3039. <https://doi.org/10.5194/bg-21-3015-2024>
- 1270 Friedlingstein, P., O’Sullivan, M., Jones, M. W., Andrew, R. M., Hauck, J., Landschützer, P., et
1271 al. (2025). Global Carbon Budget 2024. *Earth System Science Data*, 17(3), 965–1039.
1272 <https://doi.org/10.5194/essd-17-965-2025>
- 1273 Gallagher, M. E., Liljestrand, F. L., Hockaday, W. C., & Masiello, C. A. (2017). Plant species,
1274 not climate, controls aboveground biomass O₂:CO₂ exchange ratios in deciduous and
1275 coniferous ecosystems. *Journal of Geophysical Research: Biogeosciences*, 122(9),
1276 2314–2324. <https://doi.org/10.1002/2017JG003847>
- 1277 Garcia, H. E., & Keeling, R. F. (2001). On the global oxygen anomaly and air-sea flux. *Journal*
1278 *of Geophysical Research: Oceans*, 106(C12), 31155–31166.
1279 <https://doi.org/10.1029/1999JC000200>
- 1280 Gaubert, B., Stephens, B. B., Basu, S., Chevallier, F., Deng, F., Kort, E. A., et al. (2019). Global
1281 atmospheric CO₂ inverse models converging on neutral tropical land exchange, but
1282 disagreeing on fossil fuel and atmospheric growth rate. *Biogeosciences*, 16(1), 117–134.
1283 <https://doi.org/10.5194/bg-16-117-2019>
- 1284 Gelaro, R., McCarty, W., Suárez, M. J., Todling, R., Molod, A., Takacs, L., et al. (2017). The



- 1285 Modern-Era Retrospective Analysis for Research and Applications, Version 2
1286 (MERRA-2). *Journal of Climate*, 30(14), 5419–5454.
1287 <https://doi.org/10.1175/JCLI-D-16-0758.1>
- 1288 Golaz, J.-C., Larson, V. E., & Cotton, W. R. (2002). A PDF-Based Model for Boundary Layer
1289 Clouds. Part I: Method and Model Description. *Journal of the Atmospheric Sciences*,
1290 59(24), 3540–3551.
- 1291 Goto, D., Morimoto, S., Aoki, S., Patra, P. K., & Nakazawa, T. (2017). Seasonal and short-term
1292 variations in atmospheric potential oxygen at Ny-Ålesund, Svalbard. *Tellus B: Chemical*
1293 *and Physical Meteorology*, 69(1), 1311767.
1294 <https://doi.org/10.1080/16000889.2017.1311767>
- 1295 Gouretski, V., Cheng, L., Du, J., Xing, X., Chai, F., & Tan, Z. (2024). A consistent ocean oxygen
1296 profile dataset with new quality control and bias assessment. *Earth System Science Data*,
1297 16(12), 5503–5530. <https://doi.org/10.5194/essd-16-5503-2024>
- 1298 Gruber, N., Gloor, M., Fan, S., & Sarmiento, J. L. (2001). Air-sea flux of oxygen estimated from
1299 bulk data: Implications For the marine and atmospheric oxygen cycles. *Global*
1300 *Biogeochemical Cycles*, 15(4), 783–803. <https://doi.org/10.1029/2000GB001302>
- 1301 Gurney, K. R., Law, R. M., Denning, A. S., Rayner, P. J., Baker, D., Bousquet, P., et al. (2003).
1302 TransCom 3 CO₂ inversion intercomparison: 1. Annual mean control results and
1303 sensitivity to transport and prior flux information. *Tellus B: Chemical and Physical*
1304 *Meteorology*, 55(2), 555–579. <https://doi.org/10.3402/tellusb.v55i2.16728>
- 1305 Gurney, K. R., Law, R. M., Denning, A. S., Rayner, P. J., Pak, B. C., Baker, D., et al. (2004).
1306 Transcom 3 inversion intercomparison: Model mean results for the estimation of seasonal
1307 carbon sources and sinks. *Global Biogeochemical Cycles*, 18(1).



- 1308 <https://doi.org/10.1029/2003GB002111>
- 1309 Hamme, R. C., & Emerson, S. R. (2004). The solubility of neon, nitrogen and argon in distilled
1310 water and seawater. *Deep Sea Research Part I: Oceanographic Research Papers*, 51(11),
1311 1517–1528. <https://doi.org/10.1016/j.dsr.2004.06.009>
- 1312 Hamme, R. C., & Keeling, R. F. (2008). Ocean ventilation as a driver of interannual variability in
1313 atmospheric potential oxygen. *Tellus B: Chemical and Physical Meteorology*, 60(5),
1314 706–717. <https://doi.org/10.1111/j.1600-0889.2008.00376.x>
- 1315 Heimann, M., & Körner, S. (2003). *The global atmospheric tracer model TM3: Model*
1316 *description and user's manual Release 3.8a*.
- 1317 Hersbach, H., Bell, B., Berrisford, P., Hirahara, S., Horányi, A., Muñoz-Sabater, J., et al. (2020).
1318 The ERA5 global reanalysis. *Quarterly Journal of the Royal Meteorological Society*,
1319 146(730), 1999–2049. <https://doi.org/10.1002/qj.3803>
- 1320 Hintsa, E. J., Moore, F. L., Hurst, D. F., Dutton, G. S., Hall, B. D., Nance, J. D., et al. (2021).
1321 UAS Chromatograph for Atmospheric Trace Species (UCATS) – a versatile instrument
1322 for trace gas measurements on airborne platforms. *Atmospheric Measurement Techniques*,
1323 14(10), 6795–6819. <https://doi.org/10.5194/amt-14-6795-2021>
- 1324 Hockaday, W. C., Masiello, C. A., Randerson, J. T., Smernik, R. J., Baldock, J. A., Chadwick, O.
1325 A., & Harden, J. W. (2009). Measurement of soil carbon oxidation state and oxidative
1326 ratio by ^{13}C nuclear magnetic resonance. *Journal of Geophysical Research:*
1327 *Biogeosciences*, 114(G2), 2008JG000803. <https://doi.org/10.1029/2008JG000803>
- 1328 Holtslag, A. a. M., & Boville, B. A. (1993). Local Versus Nonlocal Boundary-Layer Diffusion in
1329 a Global Climate Model. *Journal of Climate*, 6(10), 1825–1842.
- 1330 Hourdin, F., Talagrand, O., & Idelkadi, A. (2006). Eulerian backtracking of atmospheric tracers.



- 1331 II: Numerical aspects. *Quarterly Journal of the Royal Meteorological Society*, 132(615),
1332 585–603. <https://doi.org/10.1256/qj.03.198.B>
- 1333 Hourdin, Frédéric, & Armengaud, A. (1999). The Use of Finite-Volume Methods for
1334 Atmospheric Advection of Trace Species. Part I: Test of Various Formulations in a
1335 General Circulation Model. *Monthly Weather Review*, 127(5), 822–837.
1336 [https://doi.org/10.1175/1520-0493\(1999\)127<0822:TUOFVM>2.0.CO;2](https://doi.org/10.1175/1520-0493(1999)127<0822:TUOFVM>2.0.CO;2)
- 1337 Hyder, P., Edwards, J. M., Allan, R. P., Hewitt, H. T., Bracegirdle, T. J., Gregory, J. M., et al.
1338 (2018). Critical Southern Ocean climate model biases traced to atmospheric model cloud
1339 errors. *Nature Communications*, 9(1), 3625. <https://doi.org/10.1038/s41467-018-05634-2>
- 1340 Ishidoya, S., Morimoto, S., Aoki, S., Taguchi, S., Goto, D., Murayama, S., & Nakazawa, T.
1341 (2012). Oceanic and terrestrial biospheric CO₂ uptake estimated from atmospheric
1342 potential oxygen observed at Ny-Ålesund, Svalbard, and Syowa, Antarctica. *Tellus B:*
1343 *Chemical and Physical Meteorology*, 64(1), 18924.
1344 <https://doi.org/10.3402/tellusb.v64i0.18924>
- 1345 Ishidoya, S., Uchida, H., Sasano, D., Kosugi, N., Taguchi, S., Ishii, M., et al. (2016). Ship-based
1346 observations of atmospheric potential oxygen and regional air–sea O₂ flux in the northern
1347 North Pacific and the Arctic Ocean. *Tellus B: Chemical and Physical Meteorology*, 68(1),
1348 29972. <https://doi.org/10.3402/tellusb.v68.29972>
- 1349 Ito, T., Cervania, A., Cross, K., Ainchwar, S., & Delawalla, S. (2024). Mapping Dissolved
1350 Oxygen Concentrations by Combining Shipboard and Argo Observations Using Machine
1351 Learning Algorithms. *Journal of Geophysical Research: Machine Learning and*
1352 *Computation*, 1(3), e2024JH000272. <https://doi.org/10.1029/2024JH000272>
- 1353 Jersild, A., Landschützer, P., Gruber, N., & Bakker, D. C. E. (2017). An observation-based global



- 1354 monthly gridded sea surface pCO₂ and air-sea CO₂ flux product from 1982 onward and
1355 its monthly climatology (NCEI Accession 0160558) [Data set]. NOAA National Centers
1356 for Environmental Information.
- 1357 Jin, X., Najjar, R. G., Louanchi, F., & Doney, S. C. (2007). A modeling study of the seasonal
1358 oxygen budget of the global ocean. *Journal of Geophysical Research: Oceans*, 112(C5),
1359 2006JC003731. <https://doi.org/10.1029/2006JC003731>
- 1360 Jin, Y., Keeling, R. F., Morgan, E. J., Ray, E., Parazoo, N. C., & Stephens, B. B. (2021). A
1361 mass-weighted isentropic coordinate for mapping chemical tracers and computing
1362 atmospheric inventories. *Atmospheric Chemistry and Physics*, 21(1), 217–238.
1363 <https://doi.org/10.5194/acp-21-217-2021>
- 1364 Jin, Y., Stephens, B. B., Keeling, R. F., Morgan, E. J., Rödenbeck, C., Patra, P. K., & Long, M. C.
1365 (2023). Seasonal Tropospheric Distribution and Air-Sea Fluxes of Atmospheric Potential
1366 Oxygen From Global Airborne Observations. *Global Biogeochemical Cycles*, 37(10),
1367 e2023GB007827. <https://doi.org/10.1029/2023GB007827>
- 1368 Jin, Y., Keeling, R. F., Stephens, B. B., Long, M. C., Patra, P. K., Rödenbeck, C., et al. (2024).
1369 Improved atmospheric constraints on Southern Ocean CO₂ exchange. *Proceedings of the*
1370 *National Academy of Sciences*, 121(6), e2309333121.
1371 <https://doi.org/10.1073/pnas.2309333121>
- 1372 Jones, M. W., Andrew, R. M., Peters, G. P., Janssens-Maenhout, G., De-Gol, A. J., Ciais, P., et al.
1373 (2021). Gridded fossil CO₂ emissions and related O₂ combustion consistent with national
1374 inventories 1959–2018. *Scientific Data*, 8(2).
1375 <https://doi.org/10.1038/s41597-020-00779-6>
- 1376 Jones, M. W., Andrew, R. M., Peters, G. P., Janssens-Maenhout, G., De-Gol, A. J., Dou, X., et al.



- 1377 (2022). Gridded fossil CO₂ emissions and related O₂ combustion consistent with national
1378 inventories 1959-2020 (Version GCP-GridFEDv2021.3) [Data set]. Zenodo.
1379 <https://doi.org/10.5281/zenodo.5956612>
- 1380 Kalnay, E., Kanamitsu, M., Kistler, R., Collins, W., Deaven, D., Gandin, L., et al. (1996). The
1381 NCEP/NCAR 40-Year Reanalysis Project. *Bulletin of the American Meteorological*
1382 *Society*, 77(3), 437–472.
- 1383 Kay, J. E., Hillman, B. R., Klein, S. A., Zhang, Y., Medeiros, B., Pincus, R., et al. (2012).
1384 Exposing Global Cloud Biases in the Community Atmosphere Model (CAM) Using
1385 Satellite Observations and Their Corresponding Instrument Simulators. *Journal of*
1386 *Climate*. <https://doi.org/10.1175/JCLI-D-11-00469.1>
- 1387 Keeling, R. F. (1988). *Development of an Interferometric Oxygen Analyzer for Precise*
1388 *Measurement of the Atmospheric O₂ Mole Fraction*. Harvard University.
- 1389 Keeling, R. F., & Shertz, S. R. (1992). Seasonal and interannual variations in atmospheric
1390 oxygen and implications for the global carbon cycle. *Nature*, 358(6389), 723–727.
1391 <https://doi.org/10.1038/358723a0>
- 1392 Keeling, R. F., Najjar, R. P., Bender, M. L., & Tans, P. P. (1993). What atmospheric oxygen
1393 measurements can tell us about the global carbon cycle. *Global Biogeochemical Cycles*,
1394 7(1), 37–67. <https://doi.org/10.1029/92GB02733>
- 1395 Keeling, R. F., Stephens, B. B., Najjar, R. G., Doney, S. C., Archer, D., & Heimann, M. (1998).
1396 Seasonal variations in the atmospheric O₂/N₂ ratio in relation to the kinetics of air-sea gas
1397 exchange. *Global Biogeochemical Cycles*, 12(1), 141–163.
1398 <https://doi.org/10.1029/97GB02339>
- 1399 Keeling, R. F., Walker, S. J., & Paplawsky, W. (2020). *Span Sensitivity of the Scripps*



- 1400 *Interferometric Oxygen Analyzer.*
- 1401 Keeling, R. F. (2019). Scripps O₂ Program Data. UC San Diego Library Digital Collections [Data
1402 set]. <https://doi.org/10.6075/J0WS8RJR>
- 1403 Keeling, R. F., Manning, A. C., McEvoy, E. M., & Shertz, S. R. (1998). Methods for measuring
1404 changes in atmospheric O₂ concentration and their application in southern hemisphere
1405 air. *Journal of Geophysical Research: Atmospheres*, 103(D3), 3381–3397.
1406 <https://doi.org/10.1029/97JD02537>
- 1407 Keeling, R.F., & Manning, A. C. (2014). Studies of Recent Changes in Atmospheric O₂ Content.
1408 In *Treatise on Geochemistry* (pp. 385–404). Elsevier.
1409 <https://doi.org/10.1016/B978-0-08-095975-7.00420-4>
- 1410 Kenneth N. S., John Mund, Ingrid T. Luijkx, Tuula Aalto, James Brice Abshire, Ken Aikin, et al.
1411 (2021). Multi-laboratory compilation of atmospheric carbon dioxide data for the period
1412 1957-2020; obspack_co2_1_GLOBALVIEWplus_v7.0_2021-08-18 [Data set]. NOAA
1413 Global Monitoring Laboratory [Data set]. <https://doi.org/10.25925/20210801>
- 1414 Knight, C. L., Mallet, M. D., Alexander, S. P., Fraser, A. D., Protat, A., & McFarquhar, G. M.
1415 (2024). Cloud Properties and Boundary Layer Stability Above Southern Ocean Sea Ice
1416 and Coastal Antarctica. *Journal of Geophysical Research: Atmospheres*, 129(10),
1417 e2022JD038280. <https://doi.org/10.1029/2022JD038280>
- 1418 Kobayashi, S., Ota, Y., Harada, Y., Ebata, A., Moriya, M., Onoda, H., et al. (2015). The JRA-55
1419 Reanalysis: General Specifications and Basic Characteristics. *Journal of the*
1420 *Meteorological Society of Japan. Ser. II*, 93(1), 5–48.
1421 <https://doi.org/10.2151/jmsj.2015-001>
- 1422 Kosaka, Y., Kobayashi, S., Harada, Y., Kobayashi, C., Naoe, H., Yoshimoto, K., et al. (2024).



- 1423 The JRA-3Q Reanalysis. *Journal of the Meteorological Society of Japan. Ser. II*, 102(1),
1424 49–109. <https://doi.org/10.2151/jmsj.2024-004>
- 1425 Krol, M., Houweling, S., Bregman, B., van den Broek, M., Segers, A., van Velthoven, P., et al.
1426 (2005). The two-way nested global chemistry-transport zoom model TM5: algorithm and
1427 applications. *Atmospheric Chemistry and Physics*, 5(2), 417–432.
1428 <https://doi.org/10.5194/acp-5-417-2005>
- 1429 Krol, Maarten, De Bruine, M., Killaars, L., Ouwersloot, H., Pozzer, A., Yin, Y., et al. (2018).
1430 Age of air as a diagnostic for transport timescales in global models. *Geoscientific Model*
1431 *Development*, 11(8), 3109–3130. <https://doi.org/10.5194/gmd-11-3109-2018>
- 1432 Landschützer, P., Gruber, N., & Bakker, D. C. E. (2016). Decadal variations and trends of the
1433 global ocean carbon sink. *Global Biogeochemical Cycles*, 30(10), 1396–1417.
1434 <https://doi.org/10.1002/2015GB005359>
- 1435 Lang, F., Huang, Y., Siems, S. T., & Manton, M. J. (2018). Characteristics of the Marine
1436 Atmospheric Boundary Layer Over the Southern Ocean in Response to the Synoptic
1437 Forcing. *Journal of Geophysical Research: Atmospheres*, 123(15), 7799–7820.
1438 <https://doi.org/10.1029/2018JD028700>
- 1439 Langenfelds, R. L. (2002). *Studies of the global carbon cycle using atmospheric oxygen and*
1440 *associated tracers*. University of Tasmania.
- 1441 Law, R. M., Peters, W., Rödenbeck, C., Aulagnier, C., Baker, I., Bergmann, D. J., et al. (2008).
1442 TransCom model simulations of hourly atmospheric CO₂: Experimental overview and
1443 diurnal cycle results for 2002. *Global Biogeochemical Cycles*, 22(3).
1444 <https://doi.org/10.1029/2007GB003050>
- 1445 Liu, Z., Ciais, P., Deng, Z., Davis, S. J., Zheng, B., Wang, Y., et al. (2020). Carbon Monitor, a



- 1446 near-real-time daily dataset of global CO₂ emission from fossil fuel and cement
1447 production. *Scientific Data*, 7(1), 1–12. <https://doi.org/10.1038/s41597-020-00708-7>
- 1448 Long, M. C., Moore, J. K., Lindsay, K., Levy, M., Doney, S. C., Luo, J. Y., et al. (2021).
1449 Simulations With the Marine Biogeochemistry Library (MARBL). *Journal of Advances*
1450 *in Modeling Earth Systems*, 13(12), e2021MS002647.
1451 <https://doi.org/10.1029/2021MS002647>
- 1452 Long, M. C., Stephens, B. B., McKain, K., Sweeney, C., Keeling, R. F., Kort, E. A., et al. (2021).
1453 Strong Southern Ocean carbon uptake evident in airborne observations. *Science*,
1454 374(6572), 1275–1280. <https://doi.org/10.1126/science.abi4355>
- 1455 Louis, J.-F. (1979). A parametric model of vertical eddy fluxes in the atmosphere.
1456 *Boundary-Layer Meteorology*, 17(2), 187–202. <https://doi.org/10.1007/BF00117978>
- 1457 Luijkx, I. T., Velde, I. R., Veen, E., Tsuruta, A., Stanislawski, K., Babenhauserheide, A., et al.
1458 (2017). The CarbonTracker Data Assimilation Shell (CTDAS) v1.0: implementation and
1459 global carbon balance 2001–2015. *Geoscientific Model Development*, 10(7), 2785–2800.
1460 <https://doi.org/10.5194/gmd-10-2785-2017>
- 1461 Maksyutov, S., Patra, P., Onishi, R., Saeki, T., & Nakazawa, T. (2008). NIES/FRCGC Global
1462 Atmospheric Tracer Transport Model: Description, Validation, and Surface Sources and
1463 Sinks Inversion. *Journal of the Earth Simulator*, 9, 3–18. <https://doi.org/10.32131/jes.9.3>
- 1464 Maksyutov, S., Oda, T., Saito, M., Janardanan, R., Belikov, D., Kaiser, J. W., et al. (2021).
1465 Technical note: A high-resolution inverse modelling technique for estimating surface CO₂
1466 fluxes based on the NIES-TM-FLEXPART coupled transport model and its adjoint.
1467 *Atmospheric Chemistry and Physics*, 21(2), 1245–1266.
1468 <https://doi.org/10.5194/acp-21-1245-2021>



- 1469 Manning, A. C., & Keeling, R. F. (2006). Global oceanic and land biotic carbon sinks from the
1470 Scripps atmospheric oxygen flask sampling network. *Tellus B: Chemical and Physical*
1471 *Meteorology*, 58(2), 95. <https://doi.org/10.1111/j.1600-0889.2006.00175.x>
- 1472 Mellor, G. L., & Yamada, T. (1974). A Hierarchy of Turbulence Closure Models for Planetary
1473 Boundary Layers. *Journal of the Atmospheric Sciences*.
1474 [https://doi.org/10.1175/1520-0469\(1974\)031<1791:AHOTCM>2.0.CO;2](https://doi.org/10.1175/1520-0469(1974)031<1791:AHOTCM>2.0.CO;2)
- 1475 Miyazaki, K., Patra, P. K., Takigawa, M., Iwasaki, T., & Nakazawa, T. (2008). Global-scale
1476 transport of carbon dioxide in the troposphere. *Journal of Geophysical Research:*
1477 *Atmospheres*, 113(D15), 2007JD009557. <https://doi.org/10.1029/2007JD009557>
- 1478 Morgan, E. J., Manizza, M., Keeling, R. F., Resplandy, L., Mikaloff-Fletcher, S. E., Nevison, C.
1479 D., et al. (2021). An Atmospheric Constraint on the Seasonal Air-Sea Exchange of
1480 Oxygen and Heat in the Extratropics. *Journal of Geophysical Research: Oceans*, 126(8),
1481 e2021JC017510. <https://doi.org/10.1029/2021JC017510>
- 1482 Naegler, T., Ciais, P., Orr, J. C., Aumont, O., & Rödenbeck, C. (2007). On evaluating ocean
1483 models with atmospheric potential oxygen. *Tellus B: Chemical and Physical*
1484 *Meteorology*, 59(1). <https://doi.org/10.1111/j.1600-0889.2006.00197.x>
- 1485 Najjar, R. G., & Keeling, R. F. (2000). Mean annual cycle of the air-sea oxygen flux: A global
1486 view. *Global Biogeochemical Cycles*, 14(2), 573–584.
1487 <https://doi.org/10.1029/1999GB900086>
- 1488 Nakanishi, M., & Niino, H. (2004). An Improved Mellor–Yamada Level-3 Model with
1489 Condensation Physics: Its Design and Verification. *Boundary-Layer Meteorology*, 112(1),
1490 1–31. <https://doi.org/10.1023/B:BOUN.0000020164.04146.98>
- 1491 Nevison, C., Munro, D., Lovenduski, N., Cassar, N., Keeling, R., Krummel, P., & Tjiputra, J.



- 1492 (2018). Net Community Production in the Southern Ocean: Insights From Comparing
1493 Atmospheric Potential Oxygen to Satellite Ocean Color Algorithms and Ocean Models.
1494 *Geophysical Research Letters*, 45, 10549–10559. <https://doi.org/10.1029/2018GL079575>
1495 Nevison, C. D., Mahowald, N. M., Doney, S. C., Lima, I. D., Van Der Werf, G. R., Randerson, J.
1496 T., et al. (2008). Contribution of ocean, fossil fuel, land biosphere, and biomass burning
1497 carbon fluxes to seasonal and interannual variability in atmospheric CO₂. *Journal of*
1498 *Geophysical Research: Biogeosciences*, 113(G1), 2007JG000408.
1499 <https://doi.org/10.1029/2007JG000408>
1500 Nevison, C. D., Mahowald, N. M., Doney, S. C., Lima, I. D., & Cassar, N. (2008). Impact of
1501 variable air-sea O₂ and CO₂ fluxes on atmospheric potential oxygen (APO) and
1502 land-ocean carbon sink partitioning. *Biogeosciences*, 5(3), 875–889.
1503 <https://doi.org/10.5194/bg-5-875-2008>
1504 Nevison, C. D., Keeling, R. F., Kahru, M., Manizza, M., Mitchell, B. G., & Cassar, N. (2012).
1505 Estimating net community production in the Southern Ocean based on atmospheric
1506 potential oxygen and satellite ocean color data. *Global Biogeochemical Cycles*, 26.
1507 <https://doi.org/10.1029/2011GB004040>
1508 Nevison, C. D., Manizza, M., Keeling, R. F., Kahru, M., Bopp, L., Dunne, J., et al. (2015).
1509 Evaluating the ocean biogeochemical components of Earth system models using
1510 atmospheric potential oxygen and ocean color data. *Biogeosciences*, 12(1), 193–208.
1511 <https://doi.org/10.5194/bg-12-193-2015>
1512 Nevison, C. D., Manizza, M., Keeling, R. F., Stephens, B. B., Bent, J. D., Dunne, J., et al. (2016).
1513 Evaluating CMIP5 ocean biogeochemistry and Southern Ocean carbon uptake using
1514 atmospheric potential oxygen: Present-day performance and future projection.



- 1515 *Geophysical Research Letters*, 43(5), 2077–2085. <https://doi.org/10.1002/2015GL067584>
- 1516 Nguyen, L. N. T., Meijer, H. A. J., van Leeuwen, C., Kers, B. A. M., Scheeren, H. A., Jones, A.
1517 E., et al. (2022). Two decades of flask observations of atmospheric $\delta(\text{O}_2/\text{N}_2)$, CO_2 , and
1518 APO at stations Lutjewad (the Netherlands) and Mace Head (Ireland), and 3 years from
1519 Halley station (Antarctica). *Earth System Science Data*, 14(2), 991–1014.
1520 <https://doi.org/10.5194/essd-14-991-2022>
- 1521 Niwa, Y., Tomita, H., Satoh, M., & Imasu, R. (2011). A Three-Dimensional Icosahedral Grid
1522 Advection Scheme Preserving Monotonicity and Consistency with Continuity for
1523 Atmospheric Tracer Transport. *Journal of the Meteorological Society of Japan. Ser. II*,
1524 89(3), 255–268. <https://doi.org/10.2151/jmsj.2011-306>
- 1525 Niwa, Y., Machida, T., Sawa, Y., Matsueda, H., Schuck, T. J., Brenninkmeijer, C. A. M., et al.
1526 (2012). Imposing strong constraints on tropical terrestrial CO_2 fluxes using passenger
1527 aircraft based measurements. *Journal of Geophysical Research: Atmospheres*, 117(D11).
1528 <https://doi.org/10.1029/2012JD017474>
- 1529 Niwa, Y., Tomita, H., Satoh, M., Imasu, R., Sawa, Y., Tsuboi, K., et al. (2017). A 4D-Var
1530 inversion system based on the icosahedral grid model (NICAM-TM 4D-Var v1.0) – Part
1531 1: Offline forward and adjoint transport models. *Geoscientific Model Development*, 10(3),
1532 1157–1174. <https://doi.org/10.5194/gmd-10-1157-2017>
- 1533 Noda, A. T., Oouchi, K., Satoh, M., Tomita, H., Iga, S., & Tsushima, Y. (2010). Importance of
1534 the subgrid-scale turbulent moist process: Cloud distribution in global cloud-resolving
1535 simulations. *Atmospheric Research*, 96(2), 208–217.
1536 <https://doi.org/10.1016/j.atmosres.2009.05.007>
- 1537 Numaguti, A., Takahashi, M., Nakajima, T., & Sumi, A. (1997). *Description of CCSR/NIES*



- 1538 *Atmospheric General Circulation Model., CGER's Supercomput. Monogr. Rep., 3 (Ch 1),*
1539 *National Institute for Environmental Studies, Tsukuba, Japan.* Retrieved from
1540 <https://inis.iaea.org/records/deac4-9ne50>
- 1541 Oda, T., Maksyutov, S., & Andres, R. J. (2018). The Open-source Data Inventory for
1542 Anthropogenic CO₂ version 2016 (ODIAC2016): a global monthly fossil fuel CO₂
1543 gridded emissions data product for tracer transport simulations and surface flux
1544 inversions. *Earth System Science Data*, 10(1), 87–107.
1545 <https://doi.org/10.5194/essd-10-87-2018>
- 1546 Parazoo, N. C., Denning, A. S., Berry, J. A., Wolf, A., Randall, D. A., Kawa, S. R., et al. (2011).
1547 Moist synoptic transport of CO₂ along the mid-latitude storm track. *Geophysical*
1548 *Research Letters*, 38(9), 2011GL047238. <https://doi.org/10.1029/2011GL047238>
- 1549 Patra, P. K., Law, R. M., Peters, W., Rödenbeck, C., Takigawa, M., Aulagnier, C., et al. (2008).
1550 TransCom model simulations of hourly atmospheric CO₂: Analysis of synoptic-scale
1551 variations for the period 2002–2003. *Global Biogeochemical Cycles*, 22(4).
1552 <https://doi.org/10.1029/2007GB003081>
- 1553 Patra, P. K., Houweling, S., Krol, M., Bousquet, P., Belikov, D., Bergmann, D., et al. (2011).
1554 TransCom model simulations of CH₄ and related species: linking transport, surface flux
1555 and chemical loss with CH₄ variability in the troposphere and lower stratosphere.
1556 *Atmospheric Chemistry and Physics*, 11(24), 12813–12837.
1557 <https://doi.org/10.5194/acp-11-12813-2011>
- 1558 Patra, Prabir K., Takigawa, M., Watanabe, S., Chandra, N., Ishijima, K., & Yamashita, Y. (2018).
1559 Improved Chemical Tracer Simulation by MIROC4.0-based Atmospheric
1560 Chemistry-Transport Model (MIROC4-ACTM). *SOLA*, 14(0), 91–96.



- 1561 <https://doi.org/10.2151/sola.2018-016>
- 1562 Peiro, H., Crowell, S., Schuh, A., Baker, D. F., O'Dell, C., Jacobson, A. R., et al. (2022). Four
1563 years of global carbon cycle observed from the Orbiting Carbon Observatory 2 (OCO-2)
1564 version 9 and in situ data and comparison to OCO-2 version 7. *Atmospheric Chemistry*
1565 *and Physics*, 22(2), 1097–1130. <https://doi.org/10.5194/acp-22-1097-2022>
- 1566 Pickers, P. A., Manning, A. C., Sturges, W. T., Le Quéré, C., Mikaloff Fletcher, S. E., Wilson, P.
1567 A., & Etchells, A. J. (2017). In situ measurements of atmospheric O₂ and CO₂ reveal an
1568 unexpected O₂ signal over the tropical Atlantic Ocean. *Global Biogeochemical Cycles*,
1569 31(8), 1289–1305. <https://doi.org/10.1002/2017GB005631>
- 1570 Pickers, P. A., Manning, A. C., Le Quéré, C., Forster, G. L., Luijkx, I. T., Gerbig, C., et al.
1571 (2022). Novel quantification of regional fossil fuel CO₂ reductions during COVID-19
1572 lockdowns using atmospheric oxygen measurements. *Science Advances*, 8(16), eabl9250.
1573 <https://doi.org/10.1126/sciadv.abl9250>
- 1574 Resplandy, L., Keeling, R. F., Stephens, B. B., Bent, J. D., Jacobson, A., Rödenbeck, C., &
1575 Khatiwala, S. (2016). Constraints on oceanic meridional heat transport from combined
1576 measurements of oxygen and carbon. *Climate Dynamics*, 47(9–10), 3335–3357.
1577 <https://doi.org/10.1007/s00382-016-3029-3>
- 1578 Resplandy, L., Keeling, R. F., Eddebbar, Y., Brooks, M., Wang, R., Bopp, L., et al. (2019).
1579 Quantification of ocean heat uptake from changes in atmospheric O₂ and CO₂
1580 composition. *Scientific Reports*, 9(1), 20244. <https://doi.org/10.1038/s41598-019-56490-z>
- 1581 Rio, C., & Hourdin, F. (2008). A Thermal Plume Model for the Convective Boundary Layer:
1582 Representation of Cumulus Clouds. *Journal of the Atmospheric Sciences*.
1583 <https://doi.org/10.1175/2007JAS2256.1>



- 1584 Rödenbeck, C., Quéré, C. L., Heimann, M., & Keeling, R. F. (2008). Interannual variability in
1585 oceanic biogeochemical processes inferred by inversion of atmospheric O₂/N₂ and CO₂
1586 data. *Tellus B: Chemical and Physical Meteorology*, 60(5), 685–705.
1587 <https://doi.org/10.1111/j.1600-0889.2008.00375.x>
- 1588 Rödenbeck, Christian, Adcock, K. E., Eritt, M., Gachkivskyi, M., Gerbig, C., Hammer, S., et al.
1589 (2023). The suitability of atmospheric oxygen measurements to constrain western
1590 European fossil-fuel CO₂ emissions and their trends. *Atmospheric Chemistry and Physics*,
1591 23(24), 15767–15782. <https://doi.org/10.5194/acp-23-15767-2023>
- 1592 Russell, G. L., & Lerner, J. A. (1981). A New Finite-Differencing Scheme for the Tracer
1593 Transport Equation. *Journal of Applied Meteorology*, 20(12), 1483–1498.
1594 [https://doi.org/10.1175/1520-0450\(1981\)020<1483:ANFDSF>2.0.CO;2](https://doi.org/10.1175/1520-0450(1981)020<1483:ANFDSF>2.0.CO;2)
- 1595 Sallée, J.-B., Shuckburgh, E., Bruneau, N., Meijers, A. J. S., Bracegirdle, T. J., & Wang, Z.
1596 (2013). Assessment of Southern Ocean mixed-layer depths in CMIP5 models: Historical
1597 bias and forcing response. *Journal of Geophysical Research: Oceans*, 118(4), 1845–1862.
1598 <https://doi.org/10.1002/jgrc.20157>
- 1599 Santoni, G. W., Daube, B. C., Kort, E. A., Jiménez, R., Park, S., Pittman, J. V., et al. (2014).
1600 Evaluation of the airborne quantum cascade laser spectrometer (QCLS) measurements of
1601 the carbon and greenhouse gas suite – CO₂, CH₄, N₂O, and CO – during the CalNex and
1602 HIPPO campaigns. *Atmospheric Measurement Techniques*, 7(6), 1509–1526.
1603 <https://doi.org/10.5194/amt-7-1509-2014>
- 1604 Satoh, M., Tomita, H., Yashiro, H., Miura, H., Kodama, C., Seiki, T., et al. (2014). The
1605 Non-hydrostatic Icosahedral Atmospheric Model: description and development. *Progress*
1606 *in Earth and Planetary Science*, 1(1), 18. <https://doi.org/10.1186/s40645-014-0018-1>



- 1607 Schuh, A. E., & Jacobson, A. R. (2023). Uncertainty in parameterized convection remains a key
1608 obstacle for estimating surface fluxes of carbon dioxide. *Atmospheric Chemistry and*
1609 *Physics*, 23(11), 6285–6297. <https://doi.org/10.5194/acp-23-6285-2023>
- 1610 Schuh, A. E., Jacobson, A. R., Basu, S., Weir, B., Baker, D., Bowman, K., et al. (2019).
1611 Quantifying the Impact of Atmospheric Transport Uncertainty on CO₂ Surface Flux
1612 Estimates. *Global Biogeochemical Cycles*, 33(4), 484–500.
1613 <https://doi.org/10.1029/2018GB006086>
- 1614 Severinghaus, J. (1995). *Studies of the terrestrial O₂ and carbon cycles in sand dune gases and*
1615 *in Biosphere 2*. Columbia University.
- 1616 Sharp, J. D., Fassbender, A. J., Carter, B. R., Johnson, G. C., Schultz, C., & Dunne, J. P. (2023).
1617 GOBAI-O₂ : temporally and spatially resolved fields of ocean interior dissolved oxygen
1618 over nearly 2 decades. *Earth System Science Data*, 15(10), 4481–4518.
1619 <https://doi.org/10.5194/essd-15-4481-2023>
- 1620 Steinbach, J., Gerbig, C., Rödenbeck, C., Karstens, U., Minejima, C., & Mukai, H. (2011). The
1621 CO₂ release and Oxygen uptake from Fossil Fuel Emission Estimate (COFFEE) dataset:
1622 effects from varying oxidative ratios. *Atmospheric Chemistry and Physics*, 11(14),
1623 6855–6870. <https://doi.org/10.5194/acp-11-6855-2011>
- 1624 Stephens, B. (2017). ORCAS Merge Products. Version 1.0. UCAR/NCAR - Earth Observing
1625 Laboratory [Data set]. <https://doi.org/10.5065/D6SB445X>.
- 1626 Stephens, B., Keeling, R., Bent, J., Watt, A., Shertz, S., & Paplawsky, W. (2021a). HIPPO-1
1627 airborne oxygen instrument. Version 2.0. UCAR/NCAR—Earth Observing Laboratory.
1628 [Data set]. <https://doi.org/10.5065/D6J38QVV>
- 1629 Stephens, B., Keeling, R., Bent, J., Watt, A., Shertz, S., & Paplawsky, W. (2021b). HIPPO-2



- 1630 airborne oxygen instrument. Version 2.0. UCAR/NCAR—Earth Observing Laboratory.
1631 [Data set]. <https://doi.org/10.5065/D65Q4TF0>
- 1632 Stephens, B., Keeling, R., Bent, J., Watt, A., Shertz, S., & Paplawsky, W. (2021c). HIPPO-3
1633 airborne oxygen instrument. Version 2.0. UCAR/NCAR—Earth Observing Laboratory.
1634 [Data set]. <https://doi.org/10.5065/D67H1GXJ>
- 1635 Stephens, B., Keeling, R., Bent, J., Watt, A., Shertz, S., & Paplawsky, W. (2021d). HIPPO-4
1636 airborne oxygen instrument. Version 2.0. UCAR/NCAR—Earth Observing Laboratory.
1637 [Data set]. <https://doi.org/10.5065/D679431D>
- 1638 Stephens, B., Keeling, R., Bent, J., Watt, A., Shertz, S., & Paplawsky, W. (2021e). HIPPO-5
1639 airborne oxygen instrument. Version 2.0. UCAR/NCAR—Earth Observing Laboratory.
1640 [Data set]. <https://doi.org/10.5065/D6WW7G0D>
- 1641 Stephens, B., Keeling, R., Bent, J., Watt, A., Shertz, S., & Paplawsky, W. (2021f). ORCAS
1642 Airborne Oxygen Instrument. Version 2.0. UCAR/NCAR - Earth Observing Laboratory.
1643 [Data set]. <https://doi.org/10.5065/D6N29VC6>
- 1644 Stephens, B., Long, M., Jin, Y., Chandra, N., Chevallier, F., Hooghiem, J., et al. (2025).
1645 Atmospheric Potential Oxygen forward Model Intercomparison Project (APO-MIP)
1646 [Data set]. UCAR/NCAR - Research Data Archive. <https://doi.org/10.5065/F3PW-A676>
- 1647 Stephens, B. B. (2025). ARSV Laurence M. Gould Atmospheric O₂ and CO₂ Measurements.
1648 Version 1.0. UCAR/NCAR - Earth Observing Laboratory [Data set].
1649 <https://doi.org/10.26023/FDDD-PC3X-4M0X>
- 1650 Stephens, B. B., Keeling, R. F., Heimann, M., Six, K. D., Murnane, R., & Caldeira, K. (1998).
1651 Testing global ocean carbon cycle models using measurements of atmospheric O₂ and
1652 CO₂ concentration. *Global Biogeochemical Cycles*, 12(2), 213–230.



- 1653 <https://doi.org/10.1029/97GB03500>
- 1654 Stephens, B. B., Keeling, R. F., & Paplawsky, W. J. (2003). Shipboard measurements of
- 1655 atmospheric oxygen using a vacuum-ultraviolet absorption technique. *Tellus B: Chemical*
- 1656 *and Physical Meteorology*, 75B, 857–878. <https://doi.org/10.3402/tellusb.v55i4.16386>
- 1657 Stephens, B. B., Gurney, K. R., Tans, P. P., Sweeney, C., Peters, W., Bruhwiler, L., et al. (2007).
- 1658 Weak Northern and Strong Tropical Land Carbon Uptake from Vertical Profiles of
- 1659 Atmospheric CO₂. *Science*, 316(5832), 1732–1735.
- 1660 <https://doi.org/10.1126/science.1137004>
- 1661 Stephens, B. B., Long, M. C., Keeling, R. F., Kort, E. A., Sweeney, C., Apel, E. C., et al. (2018).
- 1662 The O₂/N₂ Ratio and CO₂ Airborne Southern Ocean Study. *Bulletin of the American*
- 1663 *Meteorological Society*, 99(2), 381–402. <https://doi.org/10.1175/BAMS-D-16-0206.1>
- 1664 Stephens, B. B., Morgan, E. J., Bent, J. D., Keeling, R. F., Watt, A. S., Shertz, S. R., & Daube, B.
- 1665 C. (2021). Airborne measurements of oxygen concentration from the surface to the lower
- 1666 stratosphere and pole to pole. *Atmospheric Measurement Techniques*, 14(3), 2543–2574.
- 1667 <https://doi.org/10.5194/amt-14-2543-2021>
- 1668 Stohl, A., Forster, C., Frank, A., Seibert, P., & Wotawa, G. (2005). Technical note: The
- 1669 Lagrangian particle dispersion model FLEXPART version 6.2. *Atmospheric Chemistry*
- 1670 *and Physics*, 5(9), 2461–2474. <https://doi.org/10.5194/acp-5-2461-2005>
- 1671 Thompson, C., Wofsy, S. C., Prather, M. J., Newman, P. A., Hanisco, T. F., Ryerson, T. B., et al.
- 1672 (2022). The NASA Atmospheric Tomography (ATom) Mission: Imaging the Chemistry
- 1673 of the Global Atmosphere. *Bulletin of the American Meteorological Society*, 103(3),
- 1674 E761–E790. <https://doi.org/10.1175/BAMS-D-20-0315.1>
- 1675 Thompson, R., Manning, A. C., Lowe, D. C., & Weatherburn, D. C. (2007). A ship-based



- 1676 methodology for high precision atmospheric oxygen measurements and its application in
1677 the Southern Ocean region. *Tellus B: Chemical and Physical Meteorology*, 59(4), 643.
1678 <https://doi.org/10.1111/j.1600-0889.2007.00292.x>
- 1679 Thompson, R. L., Patra, P. K., Ishijima, K., Saikawa, E., Corazza, M., Karstens, U., et al. (2014).
1680 TransCom N₂O model inter-comparison – Part 1: Assessing the influence of transport and
1681 surface fluxes on tropospheric N₂O variability. *Atmospheric Chemistry and Physics*,
1682 14(8), 4349–4368. <https://doi.org/10.5194/acp-14-4349-2014>
- 1683 Tiedtke, M. (1989). A Comprehensive Mass Flux Scheme for Cumulus Parameterization in
1684 Large-Scale Models. *Monthly Weather Review*, 117(8), 1779–1800.
1685 [https://doi.org/10.1175/1520-0493\(1989\)117<1779:ACMFSF>2.0.CO;2](https://doi.org/10.1175/1520-0493(1989)117<1779:ACMFSF>2.0.CO;2)
- 1686 Tohjima, Y., Minejima, C., Mukai, H., Machida, T., Yamagishi, H., & Nojiri, Y. (2012). Analysis
1687 of seasonality and annual mean distribution of atmospheric potential oxygen (APO) in the
1688 Pacific region. *Global Biogeochemical Cycles*, 26(4), 2011GB004110.
1689 <https://doi.org/10.1029/2011GB004110>
- 1690 Tohjima, Y., Terao, Y., Mukai, H., Machida, T., Nojiri, Y., & Maksyutov, S. (2015).
1691 ENSO-related variability in latitudinal distribution of annual mean atmospheric potential
1692 oxygen (APO) in the equatorial Western Pacific. *Tellus B: Chemical and Physical*
1693 *Meteorology*, 67(1), 25869. <https://doi.org/10.3402/tellusb.v67.25869>
- 1694 Tohjima, Y., Mukai, H., Machida, T., Hoshina, Y., & Nakaoka, S.-I. (2019). Global carbon
1695 budgets estimated from atmospheric O₂N₂ and CO₂ observations in the western Pacific
1696 region over a 15-year period. *Atmospheric Chemistry and Physics*, 19(14), 9269–9285.
1697 <https://doi.org/10.5194/acp-19-9269-2019>
- 1698 Tohjima, Y., Shirai, T., Ishizawa, M., Mukai, H., Machida, T., Sasakawa, M., et al. (2024).



- 1699 Observed APO Seasonal Cycle in the Pacific: Estimation of Autumn O₂ Oceanic
1700 Emissions. *Global Biogeochemical Cycles*, 38(9), e2024GB008230.
1701 <https://doi.org/10.1029/2024GB008230>
- 1702 Truong, S. C. H., Huang, Y., Lang, F., Messmer, M., Simmonds, I., Siems, S. T., & Manton, M. J.
1703 (2020). A Climatology of the Marine Atmospheric Boundary Layer Over the Southern
1704 Ocean From Four Field Campaigns During 2016–2018. *Journal of Geophysical*
1705 *Research: Atmospheres*, 125(20), e2020JD033214.
1706 <https://doi.org/10.1029/2020JD033214>
- 1707 Tsujino, H., Urakawa, S., Nakano, H., Small, R. J., Kim, W. M., Yeager, S. G., et al. (2018).
1708 JRA-55 based surface dataset for driving ocean–sea-ice models (JRA55-do). *Ocean*
1709 *Modelling*, 130, 79–139. <https://doi.org/10.1016/j.ocemod.2018.07.002>
- 1710 Van Leer, B. (1977). Towards the ultimate conservative difference scheme. IV. A new approach
1711 to numerical convection. *Journal of Computational Physics*, 23(3), 276–299.
1712 [https://doi.org/10.1016/0021-9991\(77\)90095-X](https://doi.org/10.1016/0021-9991(77)90095-X)
- 1713 Vogelezang, D. H. P., & Holtslag, A. A. M. (1996). Evaluation and model impacts of alternative
1714 boundary-layer height formulations. *Boundary-Layer Meteorology*, 81(3), 245–269.
1715 <https://doi.org/10.1007/BF02430331>
- 1716 Watanabe, S., Miura, H., Sekiguchi, M., Nagashima, T., Sudo, K., Emori, S., & Kawamiya, M.
1717 (2008). Development of an Atmospheric General Circulation Model for Integrated Earth
1718 System Modeling on the Earth Simulator. *Journal of the Earth Simulator*, 9, 27–35.
- 1719 Wofsy, S. (2021). ATom: Merged atmospheric chemistry, trace gases, and aerosols, version 2
1720 (version 2.0). ORNL Distributed Active Archive Center. [Data set].
1721 <https://doi.org/10.3334/ORNLDAAAC/1925>



- 1722 Wofsy, S. C. (2011). HIAPER Pole-to-Pole Observations (HIPPO): fine-grained, global-scale
1723 measurements of climatically important atmospheric gases and aerosols. *Philosophical*
1724 *Transactions of the Royal Society A*, 369(1943), 2073–2086.
1725 <https://doi.org/10.1098/rsta.2010.0313>
- 1726 Wofsy, S. C. (2017). HIPPO merged 10-second meteorology, atmospheric chemistry, and aerosol
1727 data. Version 1.0. UCAR/NCAR - Earth Observing Laboratory. [Data set].
1728 https://doi.org/10.3334/CDIAC/HIPPO_010
- 1729 Worrall, F., Clay, G. D., Masiello, C. A., & Mynheer, G. (2013). Estimating the oxidative ratio of
1730 the global terrestrial biosphere carbon. *Biogeochemistry*, 115(1–3), 23–32.
1731 <https://doi.org/10.1007/s10533-013-9877-6>
- 1732 Yeager, S. G., Rosenbloom, N., Glanville, A. A., Wu, X., Simpson, I., Li, H., et al. (2022). The
1733 Seasonal-to-Multiyear Large Ensemble (SMYLE) prediction system using the
1734 Community Earth System Model version 2. *Geoscientific Model Development*, 15(16),
1735 6451–6493. <https://doi.org/10.5194/gmd-15-6451-2022>
- 1736 Zhang, G. J., & McFarlane, N. A. (1995). Sensitivity of climate simulations to the
1737 parameterization of cumulus convection in the Canadian climate centre general
1738 circulation model. *Atmosphere-Ocean*, 33(3), 407–446.
1739 <https://doi.org/10.1080/07055900.1995.9649539>